Contents lists available at ScienceDirect

International Journal of Pharmaceutics

Probing the interplay between drug saturation, processing temperature and microstructure of amorphous solid dispersions with synchrotron X-ray phase-contrast tomography

Ecaterina Bordos [a,b,*], Gunjan Das [c,d,e], Sven L.M. Schroeder [c,d,e], Alastair Florence [a,b], Gavin W. Halbert [a,b], John Robertson [a,b]

[a] CMAC, University of Strathclyde, Technology and Innovation Centre, 99 George Street, Glasgow, G1 1RD, UK
[b] Strathclyde Institute for Pharmacy and Biomedical Sciences, University of Strathclyde, 161 Cathedral Street, Glasgow G4 0RE, UK
[c] School of Chemical and Process Engineering, University of Leeds, Leeds, UK
[d] Diamond Light Source, Harwell Science and Innovation Campus, Chilton, Didcot, OX11 0DE, UK
[e] EPSRC Future Manufacturing Research Hub, CMAC, Research Complex at Harwell, Harwell Science and Innovation Campus, Chilton, Didcot, OX11 0FA, UK

ARTICLE INFO

ABSTRACT

The impact of drug saturation and processing regime on the microstructure of amorphous solid dispersions (ASDs) produced by hot-melt extrusion (HME) has been investigated. By exploring various combinations of drug loadings and processing temperatures, a range of drug saturation points were obtained by HME. The process was monitored with an in-line low-frequency Raman probe to construct the respective solubility phase diagram (i.e., solubility of crystalline drug in molten/soften polymer). The resulting ASDs were analysed with synchrotron X-ray phase-contrast micro computed tomography (Sync-XPC-μCT) in conjunction with a tailored image segmentation strategy to extract quantitative and qualitative descriptors. Despite minimal elemental variability between the drug (paracetamol) and the polymer (HPMC), Sync-XPC-μCT provided sufficient contrast to identify multiple structural domains, including drug-rich crystalline clusters, impurities, polymer-related heterogeneities and voids/pores. Supersaturated ASDs (> 20 wt% drug loading) displayed higher structural complexity and showed a plethora of highly defective API-rich crystalline domains upon ageing, which were absent in the undersaturated ASDs. Beyond its impact on the API physical state, the HME processing regime influenced the degree of homogeneity within the polymer fraction, as well as total porosity, size, shape and pore connectivity. By correlating with fundamental API-polymer solubility data, this study offers additional insight into the dynamics of the drug's solubilisation process during extrusion and the subsequent formation of microstructures within the ASD system, which have potential implications on product performance and stability.

1. Introduction

Amorphous solid dispersions (ASDs) are one of the most promising formulation strategies to enhance the oral bioavailability of poorly soluble drugs. By disrupting the crystalline lattice of the drug, these formulations reduce the energy penalty necessary to dissociate the molecules and have been shown to improve drug dissolution rate, maximise its apparent aqueous solubility, and its permeability (Giri, 2021; Hate et al., 2019; Darwich et al., 2023; Andrews et al., 2023). However, the amorphous drug form possesses an excess of free energy compared to its stable crystalline counterpart, which provides a thermodynamic driving force for physical instability (Graeser et al., 2010; Repka et al., 2013). This may reduce the solubility advantage and compromise the physical integrity of the solid dosage form, limiting

product shelf-life and therapeutic efficacy. The lack of control over the risk of phase separation and recrystallisation has limited their translation into appropriate dosage forms in marketed products. Thus, the manufacture of stable ASD systems remains challenging and often requires optimisation of formulation, manufacturing route and processing parameters to attain reliable drug product quality (Li et al., 2016).

Hot-melt extrusion (HME) is one of the most efficient ASD manufacturing processes (Butreddy et al., 2021; Patil et al., 2016; Alzahrani, 2022; Repka et al., 2008). Within the extruding apparatus, the physical mixture of crystalline active pharmaceutical ingredient (API) and polymer is subjected to intensive mixing, shear and varying temperatures along the barrel to promote the dissolution of the API in the polymer matrix. During this process the drug could be molecularly dispersed or exist as a suspended amorphous or crystalline phase. The degree of homogeneity and the number of phases present within the resultant ASD are primarily the result of the physicochemical properties of the drug and polymer used in the formulation. These dictate miscibility and solubility of the drug in the polymer matrix. However, equipment and process variables such as the screw configuration, barrel temperature, screw speed and feed rate have also been shown to impact the extent and rate of conversion of the crystalline drug into the amorphous form, as well as the mechanical properties of the ASD product (Ma, 2019; Van Renterghem, 2017; Li et al., 2015; Almotairy, 2023).

Residual crystallinity and thermal degradation are two major critical quality attributes of ASDs produced by HME (Moseson and Taylor, 2023; Butreddy et al., 2021; Evans, 2018). Due to limited residence time in the extruding apparatus, it is critical to provide an adequate level of mixing and sufficient thermal input to promote the dissolution of the API whilst avoiding thermal degradation. Thus, from an API-polymer solubility perspective (i.e., solubility of crystalline drug in molten/soften polymer) and based on kinetic and thermodynamic considerations, three processing regimes have been proposed to define the operating design space for miscible API-polymer systems during HME: (i) melting, (ii) dissolution and (iii) suspension (Moseson and Taylor, 2018). The melting regime occurs at processing temperatures that correspond to or exceed the melting point of the drug species. For most polymers this occurs at temperatures well above their glass transition temperature. Within this regime both drug and polymer have sufficient molecular mobility to achieve a molecular level of mixing with minimum mechanical input. While this assures phase homogeneity and absence of residual drug crystallinity, it can also promote substantial degradation of thermolabile substances. This apparent risk of thermal degradation and the lack of understanding of the real processing window limit the wider application of HME processing within the pharmaceutical industry. Therefore, processing under the dissolution/solubilisation regime, at temperatures between the API's melting point and the saturated solution temperature is highly desirable. In this regime, the polymer acts as a solvent and dissolves the drug below its melting temperature as a result of melting point depression phenomena (Moseson and Taylor, 2018; Zhao et al., 2011; Marsac et al., 2009; Marsac et al., 2006). However, the determination of the API solubilisation end point during extruding conditions is challenging and not routinely performed. To address this aspect, we have previously demonstrated that the saturated solubility of a crystalline drug in a polymeric matrix can be determined with in-situ low-frequency Raman spectroscopy (Bordos et al., 2019). The reported methodology uses the extinction of the spectral features corresponding to the API's crystalline lattice vibration modes to identify the drug's crystalline-to-amorphous switch and construct the temperature-composition phase diagram depicting the estimated equilibrium solubility. This can be used to define processing regimes and prevent residual API crystallinity, characteristic of the suspension regime, where crystalline API particulates are suspended in a supersaturated API-polymer mixture. The aim of this study is to further evaluate this approach by expanding our previous phase diagram and combine it with X-ray imaging analysis to assess the microstructure of the resultant ASDs.

The internal microstructure of the ASD system is an important quality attribute that directly impacts downstream processing and performance of the drug product. Although, or perhaps even because, the manufacturing process is intended to be efficient in generating a homogeneous amorphous product, the occurrence of microstructure in the product is a rather neglected aspect, with limited data available on the influence of material and process parameters on the ASD microstructure. Synchrotron X-ray phase-contrast micro-computed tomography (Sync-XPC-μCT) is an advanced imaging technique that can be used to elucidate these aspects. It allows non-invasive imaging of specimens to determine cross-sectional and three-dimensional internal structures. Sync-XPC-μCT has been extensively used in material science (Li et al., 2019; Nommeots-Nomm, et al., 2019) and biomedical research (Jafarnejad, 2019; Croton, 2018; Disney, 2019) to study weakly absorbing features in low-density objects or multiphase materials where the different components have similar X-ray attenuation coefficients. Conventional X-ray imaging methods rely mainly on X-ray absorption differences between materials for image contrast, whilst X-ray phase-contrast imaging is also sensitive to the refraction of X-rays in matter (Mayo et al., 2012). This allows for enhanced contrast, especially at the interfacial boundaries between different components within a specimen (Marathe, et al., 2019). Sync-XPC-μCT is particularly useful for low atomic number materials, such as the organic components of pharmaceutical ASDs, which have similar X-ray absorption coefficients. Thus, the specific objectives of our study were to investigate the internal structure of HME-based ASDs by means of Sync-XPC-μCT and to develop further understanding of the impact of the drug saturation level and HME processing regimes on the ASD microstructure, as well as its potential implications on ASD stability. For this purpose, solid dispersions were produced under varying saturation conditions and the process was monitored with a low-frequency Raman probe combined with multivariate data analysis to construct the temperature-composition phase diagram. The Sync-XPC-μCT investigation was coupled with a bespoke image analysis strategy to extract qualitative and quantitative descriptors for a model system of paracetamol and HPMC.

2. Materials and methods

2.1. Materials

Pharmaceutical grade form I paracetamol (PCM) powder was purchased from Mallinckrodt Inc., (Raleigh, USA). Hydroxypropyl methylcellulose (HPMC) grade Affinisol 15LV, a cellulose derivative amorphous polymer, was kindly donated by Dow Inc. (The Dow Chemical Company, now DuPont Inc., Michigan, USA). All compounds were used as received, without further purification.

2.2. Methods

2.2.1. Blending
Binary mixtures of crystalline PCM and HPMC were prepared at mass ratios of 10 wt%,

25 wt %, 35 wt%, 50 wt% and 70 wt% using a bin blender (AgiBlend MB015AB Blender, Pharmatech, Warwickshire, UK) with a 1 l vessel. Each formulation was blended for 20 min at a set blend speed and agitation of 25 rpm and 100 rpm, respectively. Prior to blending, materials were sieved through a 710 μm mesh to remove powder agglomerates.

2.2.2. Preparation of amorphous solid dispersions by hot-melt extrusion (HME)
HME was performed with an 11 mm co-rotating twin-screw extruder (Process 11, 40: 3/4 L/D Thermo Fisher Scientific, Karlsruhe, Germany) in combination with a loss-in-weight gravimetric feeder (Brabender Gravimetric feeder DDW-MD-MT, Brabender Technologie, Duisburg, Germany). A constant screw speed of 100 rpm and a feed rate of 0.1 kg/h

were employed. The extruding apparatus is formed of 8-barrel sections and a die zone (refer to schematics in Figure S1). Barrel section 1 is permanently cooled, whilst sections 2 and 3 were at set-point values of 50°C and 100°C, respectively, to prevent blockage of the feeding zone. Barrel sections 4 to 8 and the die zone were operated at the same set-point temperature values, which varied according to the drug-polymer composition as reported in Table 1. The chosen temperature range was intended to create three distinct processing regimes: melting, dissolution and suspension to assess the effect of processing temperature on the ASD microstructure. Product melt temperature was monitored with a pressure–temperature probe (Terwin Instruments Ltd., Bottesford, UK) immersed in the API-polymer mixture in the die section. Processing pressure, screw speed, barrel temperature and motor torque were recorded with CX-supervisor software (Omron Corporation, UK). The temperature values measured by the melt probe were constantly higher than the reported set-point values due to the heat generated from shear. However, within this work we denote temperature values as set-point temperature values to demark each processing regime and facilitate inter-sample comparison. For the actual product melt temperature refer to Table 1. Collected extrudates were allowed to cool to ambient temperature by natural convection prior to pelletisation (Thermo Scientific™ VariCut Pelletizer, Thermo Fisher Scientific, UK) and storage until further analysis. Sync-PC-μCT analysis of these samples took place within a week of HME processing.

Extruded materials from our previous work (Bordos et al., 2019), were used for preliminary Sync-XPC-μCT tests. For this purpose, the following compositions were used: 10 wt%, 20 wt%, 25 wt% and 35 wt% drug loading. Additionally, a 50 wt% drug loading and a pure polymer formulation were also prepared. These samples were processed with a 16 mm twin-screw extruder (Eurolab 16, 40:1 L/D Thermo Fisher Scientific, Karlsruhe, Germany) at a set-point barrel temperature of 150 °C, with exception of the pure polymer formulation that was extruded at a set-point of 180 °C due to viscosity limitations. Samples were stored in sealed plastic bags at ambient conditions and aged for 6 months prior to the tomographic tests.

2.2.3. Api-polymer solubility determination

Low-frequency Raman spectroscopy was used to determine the API-polymer phase equilibria during extrusion by employing the methodology outlined in our previous work (Bordos et al., 2019). Briefly, the underlying premise is that by monitoring the API's crystalline-amorphous switch it is possible to gain access to the saturated solution temperature (T_s) (i.e. the API dissolution end point temperature). This is done by monitoring the API's crystalline lattice vibration modes present in the low-frequency Raman region (< 200 cm^{-1}). Crystalline PCM form I has three main peaks at 32, 56, and 89 cm^{-1} (Nanubolu and Burley, 2012), which are absent in the amorphous drug form and thereby, provide the basis to monitor the presence/absence of crystalline API.

Spectral data were acquired with a Terahertz (THz)-Raman probe (TR Probe, Ondax, USA) immersed into the API-polymer mixture in the die section. This device employs ultra-narrow-band notch filters to suppress Rayleigh scattering and provide access to the low-frequency Raman region. Data was acquired in reflection mode with a wavelength stabilized excitation source of 785 nm (CleanLine™ Laser Module, Ondax, USA) operating at 70mW power. The backscattered light was captured by an RXN 1 spectrometer (Kaiser Optical Systems Inc., USA) equipped with a cooled CCD detector. Data was continuously acquired during experimentation with Holograms v4.1 over the -20 cm^{-1} – 1930 cm^{-1} spectral range and included dark subtraction and cosmic ray filter. An exposure time of two seconds and three spectral accumulations were employed. Spectral pre-processing was performed with PharmaMV Development v5.2 (Perceptive Engineering Ltd., Daresbury, UK) applying Whittaker smoothing and standard normal variate (SNV) for baseline effect removal and normalisation, respectively. A principal component analysis (PCA) method was applied to the low-frequency region to interpret spectral variations using Origin Pro software (Origin Pro 2018b, OriginLab Corporation, USA).

2.2.4. Differential scanning calorimetry (DSC)

DSC experiments were performed on a DSC 214 Polyma differential scanning calorimeter (Netzsch-Geratebau GmbH, Germany) under a helium environment (purge 1 = 40 ml/min, purge 2 = 60 ml/min). Samples of 3–5 mg were weighed and crimped in 25 μL aluminium pans with pierced lids. A single heating cycle from 0 °C to 180 °C at a heating rate of 20 °C/min was employed to assess the presence of residual drug crystallinity or phase separation at each processing condition.

2.2.5. X-ray diffraction (XRD)

XRD was also performed to analyse the crystalline character of the extrudates immediately after extrusion. Data was collected on a Bruker AXS D8 Advance transmission diffractometer equipped with θ/θ geometry and primary monochromated radiation (Cu K$_{\alpha1}$, λ = 1.54056 Å). Pelletised materials were placed on an automated multiposition x-y sample stage on top of a polyimide film (Kapton, 7.5 μm thickness) and analysis was performed in the angular range of 4-35° 2θ with a 0.017° 2θ step size and 2 s per step count time.

2.2.6. Synchrotron X-ray phase contrast micro computed tomography (Sync-XPC-μCT)

X-ray tomography experiments were performed at the Diamond-Manchester Imaging Branchline I13-2 of Diamond Light Source (DLS, Didcot, UK). This beamline offers a small source size and a long distance between the synchrotron source and the sample (250 m), which results in partially-coherent illumination at the sample position. In combination with ample space available to adjust the propagation distance, it reunites optimum conditions for generating in-line phase contrast for edge enhancement of weakly absorbing features (Rau, 2017).

Experiments were conducted in a near-parallel geometry using a filtered polychromatic 'pink' beam with a peak energy of 23 keV. The process of generating the polychromatic 'pink' beam is described in detail elsewhere (Marathe, et al., 2019; Rau, et al., 2019). Pelletised materials were transferred to polyimide Kapton tubes (OD = 6.0 mm and ID = 5.85 mm, GoodFellow Cambridge, UK) and attached to a manual goniometer mounted on perpendicular linear stages (Newport Corp.,

Table 1
Hot-melt extrusion experimental conditions.

Drug loading (wt %)	Process set temperature (°C)[a]	Processing regime[b]	Measured product melt temperature (°C)[c]
10	180	M	193 ± 0.9
	150	D	158 ± 2.5
	130	D	136 ± 2.3
20	180	M	193.5 ± 0.34
	150	D	155 ± 3.5
	130	D	137.3 ± 2.7
35	180	M	192.5 ± 0.5
	145	D	153 ± 0.4
	140	S	147 ± 0.48
	135	S	142 ± 0.9
50	180	M	191.9 ± 0.2
	155	D	164.2 ± 0.4
	150	S	159.7 ± 0.46
	145	S	153 ± 0.98
70[d]	180	M	190 ± 0.99
	160	D	169 ± 0.4
	155	S	163 ± 0.3
	150	S	158 ± 0.23

[a] Refers to set-point temperature values of barrel sections 4 to 8 and the die zone.
[b] M: melting regime, D: dissolution regime and S: suspension regime.
[c] Steady state temperature values (average ± standard deviation).
[d] For this composition, the measured product melt temperature in the dissolution regime was very close to the API's T_M, therefore, it was excluded from the tomography study.

USA) as illustrated in Fig. 1. For the preliminary tests, individual pellets were mounted on cellulose sample holders. In all cases, an Aerotech ABRT-260 rotation stage (Aerotech Inc., USA) was used to rotate the samples at equally-spaced angles over 180° of continuous rotation with an exposure time of 80 ms per projection. A total of 2158 projections were acquired for each sample. Raw projection data was collected by a pco.edge 5.5 (PCO AG, Germany) detector (sCMOS image sensor of 2560 × 2160 pixels and 6.5 µm pixel size) mounted on a visual light microscope of variable magnification. Data were acquired with a 4x objective coupled to a 100 µm LuAg:S021 scintillator, providing an effective pixel size of 0.81 µm. Slits were used to restrict the beam outside the field of view to limit sample exposure and reduce noise arising from scintillator defects. The sample-to-detector distance was optimised to generate in-line phase-contrast while minimising edge blurring and the best absorption/propagation contrast ratio was obtained at a distance of 51 mm (Figure S2).

2.2.7. Tomographic reconstruction

Data were reconstructed using the filtered back projection algorithm implemented in the DLS software platform SAVU 2.2 (Wadeson and Basham, 1610). All images were corrected for zingers and subjected to flat and dark-field corrections. An additional correction step was employed to reduce ring artefacts and correct the in-plane tilt of 0.072° that occurred during experimentation. A single distance propagation-based phase contrast filter was also applied with ANKAphase (Weitkamp et al., 2011) employing the Paganin algorithm with a δ/β ratio of 85. This step helped improve the grey level of separation between sample and background despite partially enhancing the ring artefacts.

2.2.8. Image analysis

Image processing and analysis strategies were implemented in MATLAB (2018b, MathWorks, USA) with a custom-made segmentation algorithm developed for this study. This process aimed to partition the images into main regions of interest (ROIs) to enable extraction of quantitative and qualitative morphological descriptors.

Images at each processing step are shown in Fig. 2. To increase the discriminative efficiency of the segmentation algorithm, the polyimide Kapton tube and surrounding air were removed by defining a conservative ROI inside the tube (Fig. 2.b). The contrast of the cropped images was enhanced using a contrast adjustment step which combined histogram equalization and image intensity adjustment (Fig. 2.c and 2.d, respectively). Thresholding and binarisation (Fig. 2.e) was performed with Otsu's automated global thresholding method to maximise inter-class variance between foreground and background pixel classes (Otsu, 1979). Background noise was iteratively removed with a series of area and image opening morphological operations. First, all connected components with fewer than 1000 pixels (value ≪ to the pellet minimum area) were removed with area opening operations to discard major noise regions (Fig. 2.f). Then, the small contaminant regions connected to the pellets' outer limits were eliminated with an image opening operation employing a 30 pixel 'disk' structuring element (Fig. 2.j). Foreground noise was removed by inverting the contrast of the image and applying an area opening morphological operation to remove all blank regions under 3 pixels (Fig. 2.g to 2.i). There is no standard quality indicator for image segmentation and the most widely used method to assess its effectiveness is a subjective visual inspection (Zhang et al., 2008). Hence, at each step, the binarised images were superimposed to the reference unprocessed tomograms. This allowed visualisation of the segmentation results before further processing, ensuring the preservation of the delimitations of the pellets' borders and overall shape conservation. The need to enhance quality metrics for image segmentation has been highly recognised in recent years (Maier-Hein, et al., 2024; Hirling, et al., 2023). However, the lack of readily available and reliable information on these metrics still poses a significant challenge in image analysis (Reinke, et al., 2024).

To isolate the pores, a pixel-based arithmetic operation was applied to the clean binary images to subtract the solid fraction comprised between the pellets' outer perimeter and that of the "holes" (i.e. pores). After applying a filling algorithm, the pore corresponding areas were obtained (Fig. 2.m). The Euclidean distance transform and the watershed segmentation were applied to separate potential touching pore bodies and allow subsequent analysis on each individual pore. Extracted information comprised pore size and shape descriptors. Porosity was defined as the ratio of the total pore area to the whole nominal area of the pellets, including porosity. Calculations were made for a minimum of 750 successive images for each sample. The NaCl particulates (a known polymer impurity) were isolated by partially opening the connected foreground components present in Fig. 2.f with an 11x13 pixel matrix (Fig. 2.n). Once extracted these were characterised in terms of total percentage and size distribution. Fig. 2.o shows the overlay of the NaCl particulates, pores and API-polymer amorphous matrix.

To access local voxel (cubic pixel) neighbourhood information and mitigate directional bias resulting from a 2D 'slice-by-slice' segmentation, a 3D array of the segmented binary images was created. Each connected object within this array was identified and labelled. The watershed algorithm was then reapplied to separate touching objects in 3D. Fig. 3 shows the 3D volume renderings of the solid fraction, pores and NaCl clusters resulting from this approach. The eigenvectors, eigenvalues, Euler angles, volume and surface area of each pore were
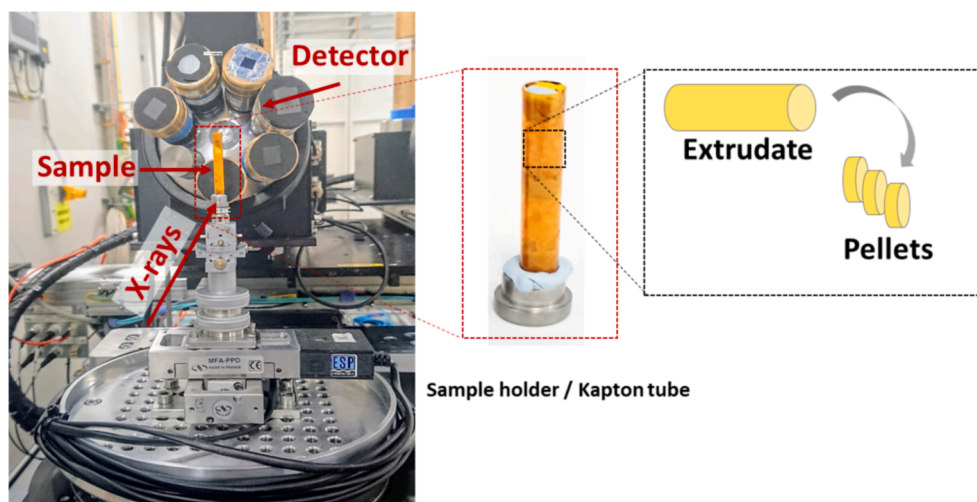

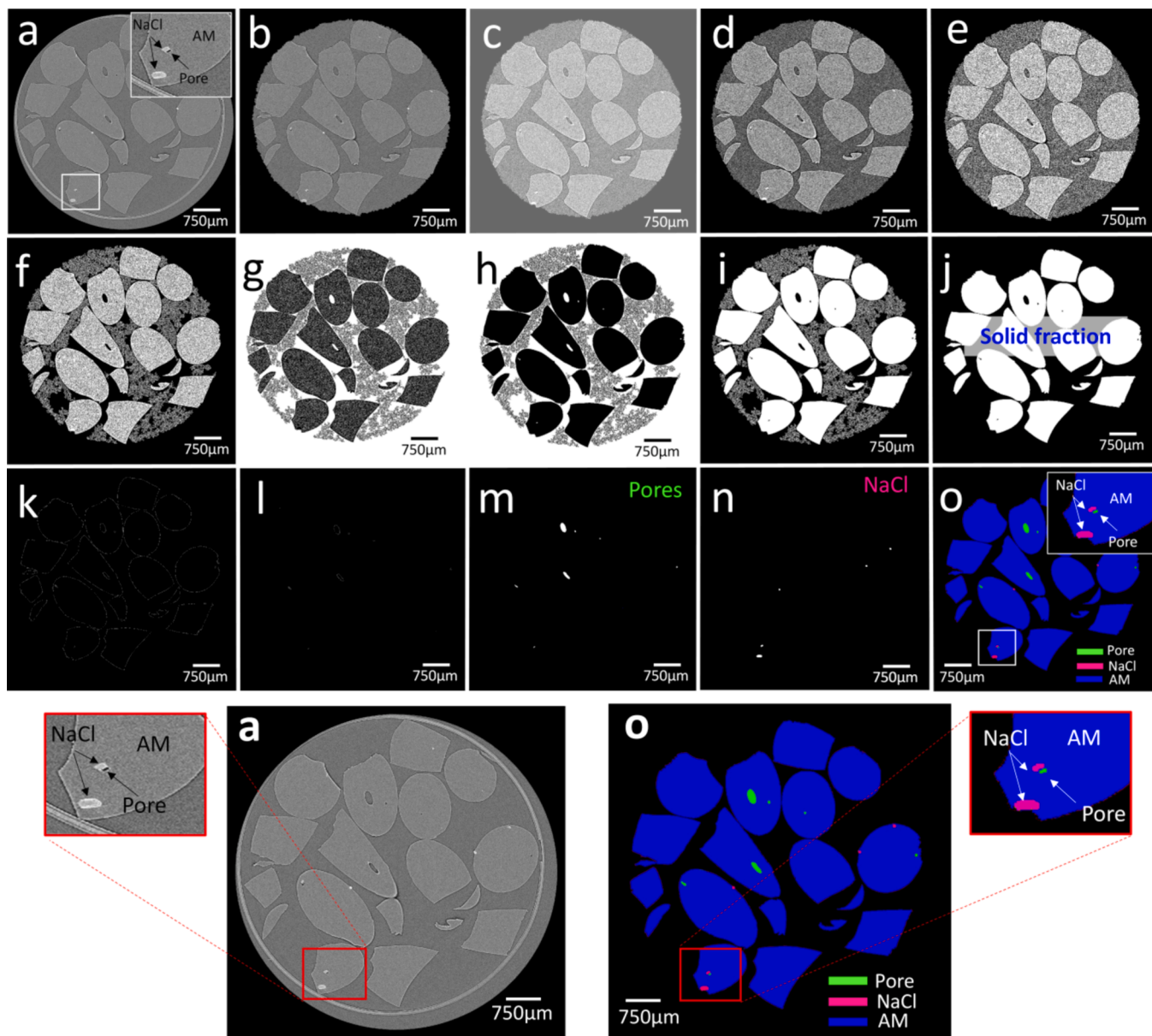**Fig. 1.** Experimental set-up illustrating the sample presentation geometry.

Fig. 2. 2D Image processing sequence: a) raw unprocessed image; b) cropped image defining the region of interest inside the Kapton tube; c) to d) gray-scale images after histogram equalization and intensity adjustment, respectively; e) binary image after thresholding and binarisation: white – foreground (pellets), black – background/noise (empty space inside the Kapton tube); f) binary images after partial background noise removal; g) to h) contrast-inverted images and foreground noise removal; i) image after foreground noise removal; j) "clean" final binary images after the second background noise removal step; k) pellet outer and inner perimeter; 1 l) pellet inner perimeter delimiting the pores; m) "filled" pore area; n) isolated NaCl particles; o) overlay of isolated NaCl clusters, pores and amorphous matrix (AM).

extracted employing the regionprops3 functionality available in Matlab (MATLAB regionprops3, xxxx). This data is obtained from the ellipsoid with matching image moments as the object. Porosity was recalculated as the volumetric percentage and results were compared to the area ratio measurements resultant from the 2D segmentation. The sphericity index (*S*) was calculated as the ratio of the nominal surface area (surface area of a sphere having the same volume as the pore) to the actual surface area of the pore as defined by Wadell:

$$S = \frac{\sqrt[3]{36\pi V_p}}{s_P} \tag{1}$$

where V_p and S_p are the pore volume and pore surface area, respectively. Here, pore volume is defined as the number of voxels present in the segmented pore region and pore surface area as the surface area of the

segmented pores in pixels. It should be noted that sphericity is a dimensionless measure of how spherical a 3D shape is, and it has a maximum value of 1 for a sphere and it decreases for non-spheroidal shapes. The pores were further characterised in terms of shape and orientation. The main orientation of a pore is given by the eigenvector with the highest eigenvalue and the ratios between the eigenvalues provide shape descriptors of the pore (Axelsson and Svensson, 2010; Markl, 2017). Hence, for shape analysis, the classification approach proposed by S. Blott and K. Pye (Blott and Pye, 2008) was adapted to assign particles to form classes based on the elongation (*E*) and flatness (*F*) ratios that are calculated as:
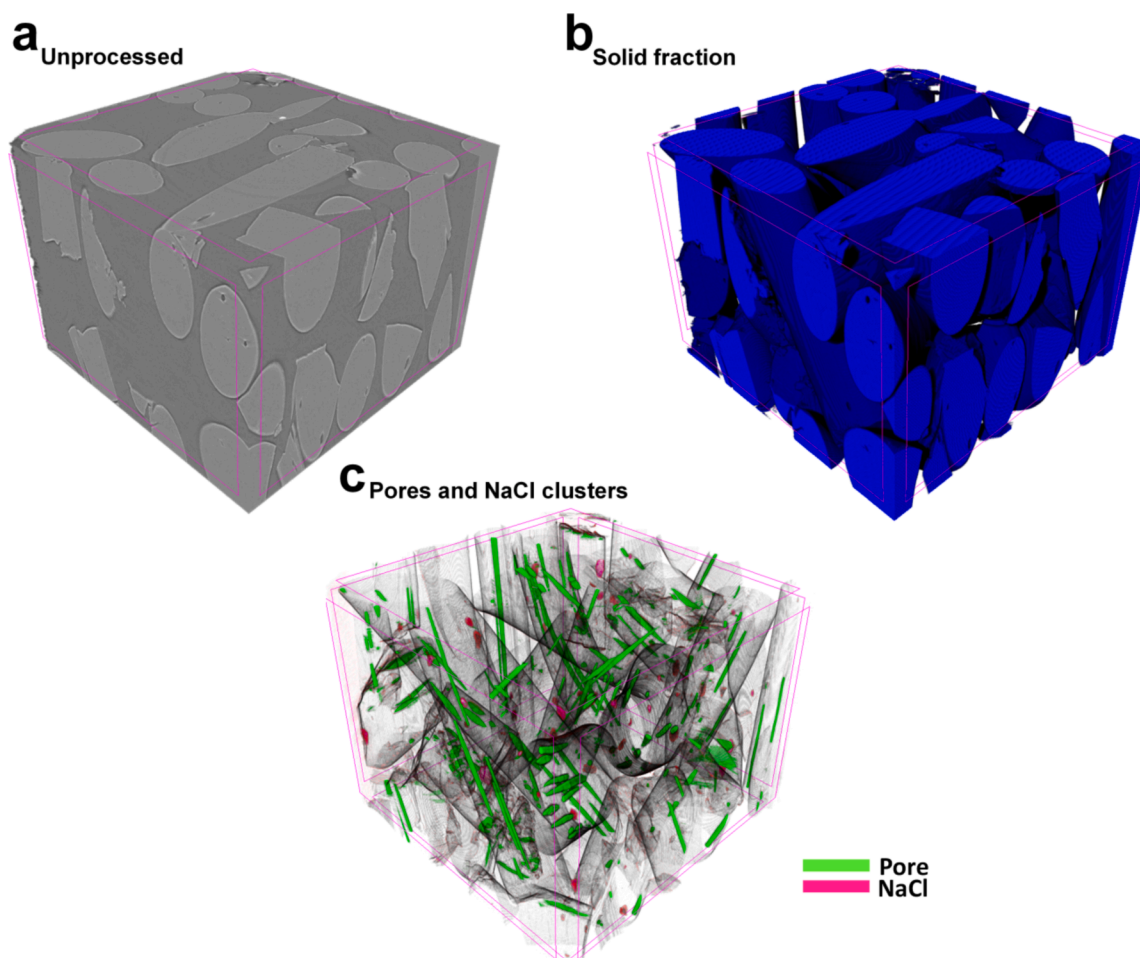
$$E = \frac{\lambda_2}{\lambda_1} \tag{2}$$

Fig. 3. Example of the 3D segmentation within a 4000 x 4000 x 4000 μm section. a) Unprocessed image, b) segmented solid fraction and c) segmented pores and NaCl particulates.

$$F = \frac{\lambda_3}{\lambda_1} \tag{3}$$

where λ_1, λ_2 and λ_3 are the largest, second largest and smallest eigenvalues respectively. For 3D visualisation, image stacks were imported into CTvox (version 3.2.0, Bruker, Kontich, Belgium).

2.2.9. Surface area measurement by N2 physisorption

Characterisation of the surface of the pellets was performed by N_2 gas physisorption with an Autosorb IQ Model 6 (Quantachrome Instruments, Florida, United States). Samples were transferred to 9 mm cells and degassed at 40 °C for 48 h prior to analysis. Measurements were conducted at 77.4 K employing an equilibration time setting of 3 min. A total of 41 data points were acquired for producing both adsorption and desorption isotherms. Data analysis was performed with the Non-Local Density Functional Theory (NLDFT) method employing the calculation model of N_2 at 77 K on carbon (slit pore).

3. Results

3.1. Effect of HME processing regime on the physical state of the API

Three extruding regimes (i.e., melting, dissolution and suspension) were employed to produce solid dispersions with varying degrees of drug saturation and structural complexity by extruding above, at and below the API's melting point. Low-frequency Raman spectroscopy confirmed the amorphous state of the API in the melting and dissolution regimes. Under these regimes only a broad amorphous shoulder with

peak maxima at 12 cm^{-1} is seen. This spectral feature arises from contributions generated from the vibrational density of states, the Boson peak and the quasi-elastic scattered radiation of both amorphous polymer and drug (Kirillov and Kolomiyets, 2001; Larkin et al., 2015). Although highly debated, the precise origin of this signal it is still not well undertood by modern physics (Taraskin et al., 2006; Terao, 2018) but it has been associated with the collective motions of atoms within the short / intermediate range order and overall molecular mobility (Bērziņš et al., 2020). Conversely, in the suspension regime residual crystallinity was observed as a result of processing below the saturated solution temperature (Ts). Residual crystallinity is determined by the presence of spectral bands characteristic of crystalline PCM form I at 32, 51 and 85 cm^{-1} (Nanubolu and Burley, 2012) (see Fig. 4.a).

Principal component analysis of the spectral data showed that two principal components (PCs) suffice to classify the data into distinct groups according to the processing temperature and to describe over 98 % of data variance (see Fig. 4.b). PC1 captures the signals arising from the amorphous band at 12 cm^{-1}, while PC2 captures the API's crystalline lattice vibration modes at 32, 51 and 85 cm^{-1}, as illustrated by the loadings analysis (Fig. 4.c). The disapereance of the API's crystalline lattice vibration modes upon solubilisation resulted in a change in the PC2 scores, transitioning from negative to positive values. Compared to our previous work, this provided a more rational approach for distinguishing between HME processing conditions containing amorphous and crystalline API.

The temperature-composition phase diagram displayed in Fig. 4. d was obtained from the PCA outputs of all compositions. It shows the
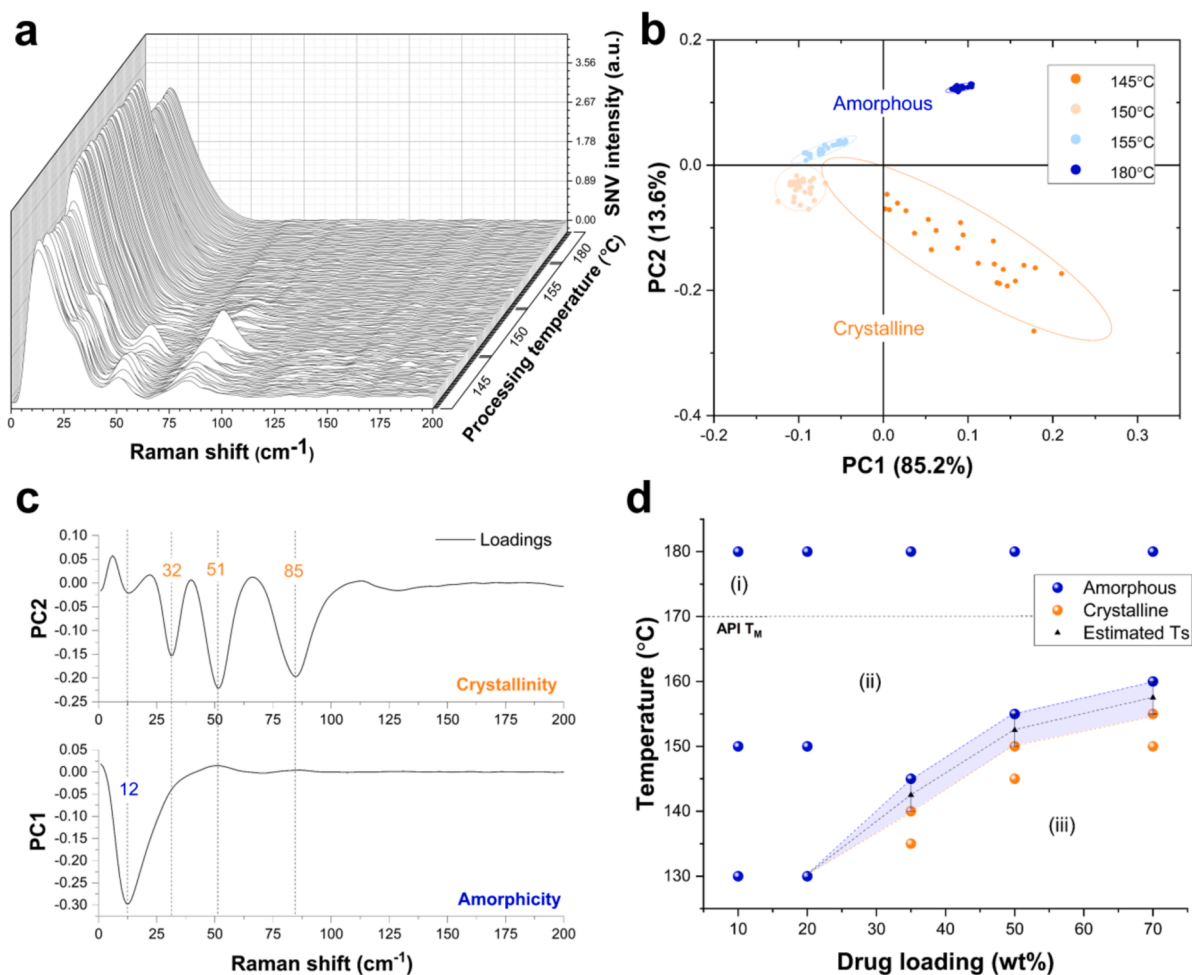
Fig. 4. API-polymer solubility determination. a) Low-frequency Raman spectral data with b) the respective PCA outputs for the 50 wt% system, c) PCA loadings plot and d) API-polymer solubility phase diagram determined from the PCA outputs. In figure d), region (i) depicts the HME melting regime, region (ii) demarks the dissolution regime and region (iii) highlights the suspension regime.

API's amorphous and crystalline temperature coordinates, as well as the estimated equilibrium temperature (with an error margin of at least ± 2.5°C). Spectral data for each individual drug loading is shown in Figure S3 along with the respective PCA analysis. Overall, residual crystallinity was only found > 20 wt% drug loading. At and below this threshold composition there was no crystallinity detected during extrusion. This is in good agreement with our previous work sugesting a solid solution capacity of ~ 20 wt% for this drug-polymer system (i.e., compositions > 20 wt% are supersaturated) (Bordos et al., 2019). However, despite the amorphous state of the drug in HME regimes (i) and (ii), these results do not assure formation of homogeneous ASDs. Therefore, there is scope for Sync-XPC-μCT to probe microstructural differences between the two amorphous regimes.
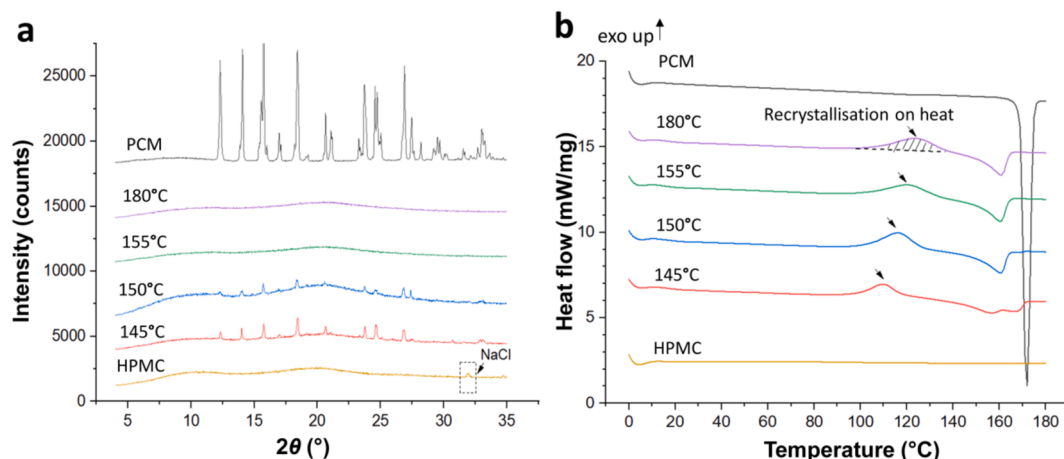

Fig. 5. A) xrd and b) dsc analysis of the 50 wt% system processed under all extruding regimes. As a reference, raw PCM and HPMC results are also shown.

3.2. XRD and DSC analysis

XRD confirmed the amorphous character of the drug in regimes (i) and (ii), as well as its crystalline state in regime (iii). As an example, Fig. 5.a shows the XRD results for the 50 wt% system. Diffraction peaks corresponding to crystalline PCM form I are seen at 145°C and 150°C (suspension regime), while amorphous halos are present at 155°C and 180°C (dissolution and melting regimes, respectively). The same trend was observed for the remaining compositions, as displayed in Figure S4. In the lower drug loading systems, an aditional diffraction peak corresponding to NaCl is seen at 2θ = ~32°. This is a known impurity present in polymer and will be further adressed in section 3.5.

DSC analysis (refer to Fig. 5.b) displayed recrystallisation exotherms within the temperature range of 109–120.5°C at all extruding temperatures as a result of exposure to heat during the measurement. This indicated partial recrystallisation to PCM form II, evidenced by the respective melting endotherm at ~ 156.6—160.0°C. For the compositions processed within the suspension regime an additional melting endotherm at ~ 168.8°C confirmed residual crystallinity of PCM form I. The same recrystallisation trend was seen for all compositions above 20 wt% drug loading, suggesting supersaturation and instability upon exposure to heat after extrusion (Figure S4). Conversely, compositions at and below 20 wt% drug loading, exhibited no melting endotherms or recrystallisation exotherms at any extruding temperatures, indicating these systems are stable. This supports the 20 wt% drug loading as the critical treshold concentration dividing compositions between stable and metastable after extrusion. Adittionally, the presence of a single glass transition temperature in the DSC thermograms suggests phase
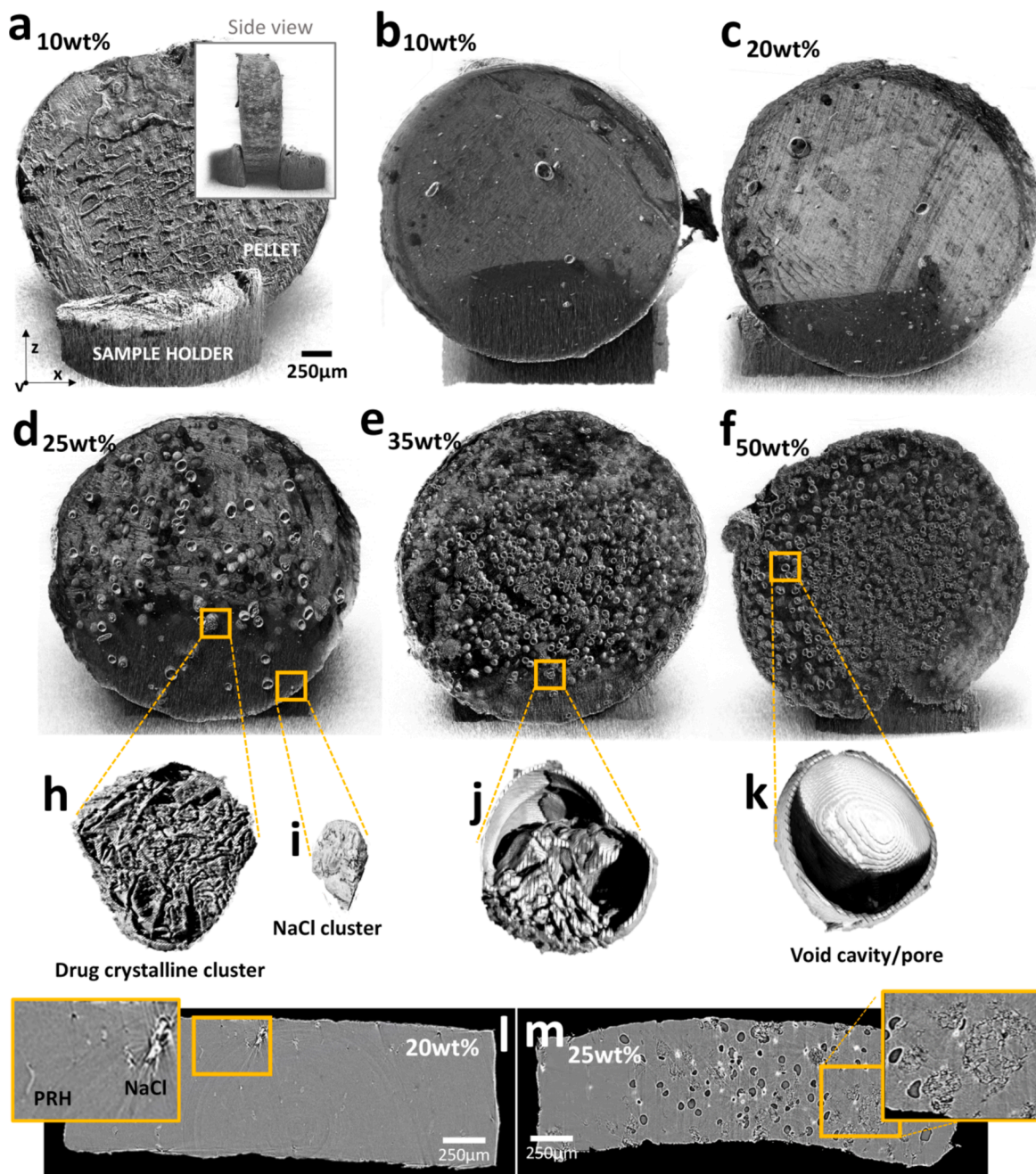

Fig. 6. 3D volume renderings and 2D cross-sections of the 6-months aged pellets. In figures b) to f) the ASD outer surface and the homogenous solid fraction corresponding to the amorphous matrix were made transparent to enable visualisation of existing bulk heterogeneities. Figure h) to k) display the main structural domains identified within the solid dispersions.

miscibility at the tested drug-loadings.

3.3. Structural characterisation of ASDs by phase contrast tomography

The potential of using Sync-XPC-μCT to probe the inner structure of HME-based ASDs was first investigated in the preliminary study where 6 months-aged samples were analysed. Fig. 6 shows 2D cross-sections and 3D volume renderings of the reconstructed data. Despite similar elemental composition of the drug and polymer used in the formulation, sufficient contrast was obtained to identify multiple structural domains within the amorphous matrix of the pellets: drug-rich crystalline domains, impurities (NaCl), polymer-related heterogeneities (PRH) and void cavities/pores, which will be discussed separately in the following sections. Remarkably, surface related phenomena such as sharkskin defects and increased roughness at the cut cross-sectional surfaces were also visualised in detail (see Fig. 6.a). Drug loadings above the assumed solid solution capacity (i.e., supersaturated and metastable ASDs) displayed higher structural complexity, containing highly defective API-rich crystalline domains and abundant pores (Fig. 6.d to 6.f). This was in stark contrast to the relatively homogeneous matrix, which is almost devoid of pores (Fig. 6.b and 6.c). The drug-rich crystalline clusters had a size range between 4 and 430 μm in diameter and were dispersed within both the solid and the porous fractions of the amorphous matrix. This size range is smaller than the average size (~400 μm) of the starting
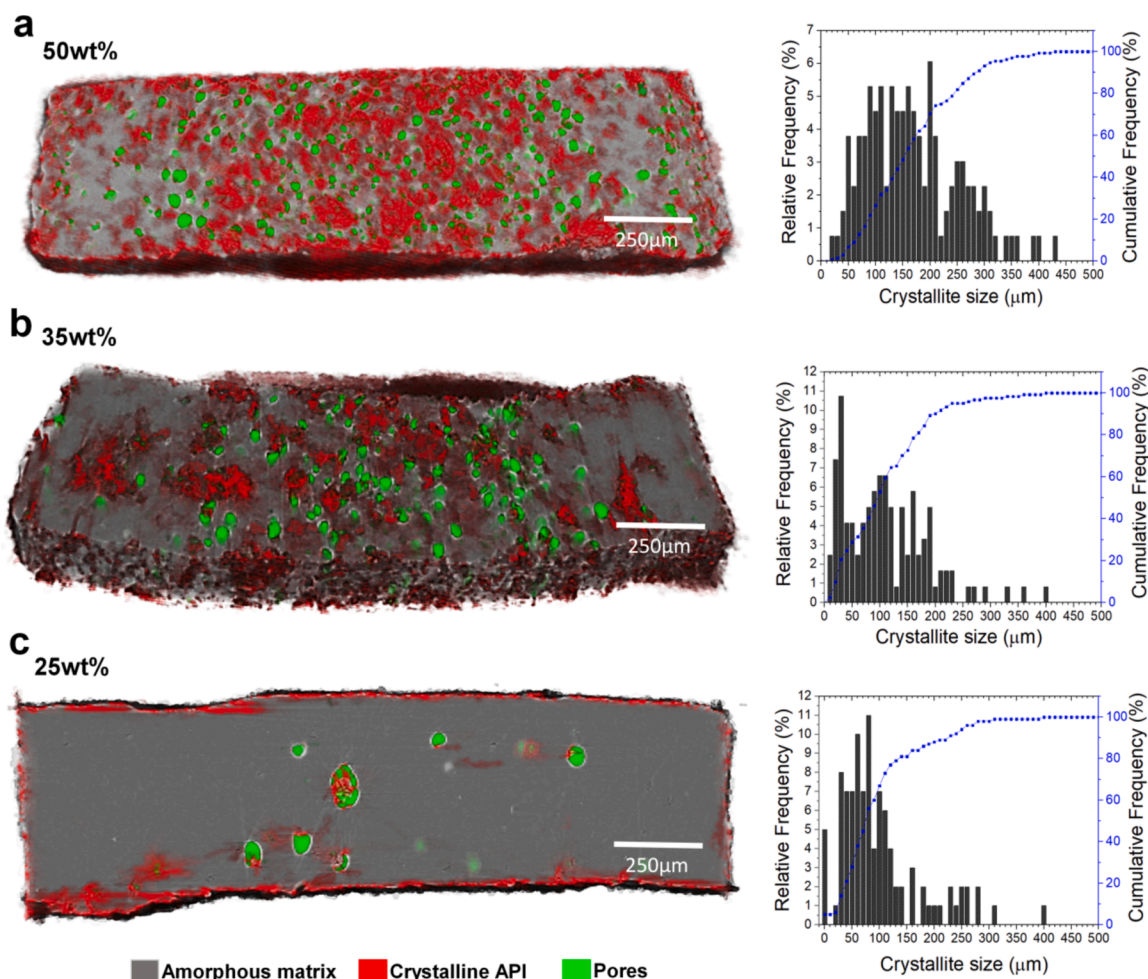
Drug-loading (%)	Porosity (%)	Fracture area (%)	API-rich crystalline area (%)[a]	Amorphous matrix area (%)[b]
50	10.32 ± 0.38	9.51 ± 1.06	39.37 ± 3.29	50.30 ± 3.41
35	7.79 ± 1.06	7.34 ± 2.25	28.34 ± 6.47	63.85 ± 6.75
25	1.46 ± 0.25	1.9 ± 1.8	9.83 ± 6.39	88.83 ± 6.47
20	1.54	----	----	----
10	1.01	----	----	----

a - derived from the fracture regions after a 5 pixels dilation operation
b - obtained from the total area after porosity and API-rich crystalline area subtraction

Fig. 7. API-rich crystalline clusters extracted from the morphological-based segmentation. a) To c) overlay of segmented pores and crystalline API clusters superimposed to the raw unprocessed images, with the respective crystallite size. d) Quantification of total porosity, fracture regions, API-rich crystalline clusters and amorphous matrix area (average ± standard deviation, n = 200 tomograms).

crystalline API material (see section 3.4 for further details). These clusters displayed a highly defective structure with multiple interface boundaries and channels that could have both intrinsic (related to the as received crystalline material) and mechanical origins induced by the HME process. In the context of API-polymer dissolution mechanism, this type of fragmented structure supports the defect site-driven dissolution and fragmentation model in addition to diffusion as proposed by Moseson *et al.* (Moseson, 2019) Nevertheless, given the long time lapse between ASD manufacture and Sync-XPC-µCT analysis for these samples, the observed crystalline drug clusters could be the result of growth of residual crystalline nuclei (i.e *.,* undissolved API at 50 wt% drug loading) or nucleation and growth from the supersaturated amorphous matrix (at 25 wt% and 35 wt% drug loadings).

3.4. Analysis of the API-rich crystalline clusters

With exception of the NaCl clusters, there was little discernible difference between the grayscale values of the structural domains identified within the solid fraction. This hampered extraction and quantification of the crystalline API clusters based on intensity threshold strategies. As an alternative approach, the characteristic interface boundaries present within the crystalline API domains were used as a morphological marker for segmentation. These were segregated from the remaining parts of the image by subtracting the isolated porous fraction from the original images. Considering that the drug-rich crystalline clusters extend around and between the boundary planes, a dilation operation was applied to add pixels to the boundaries of the fracture planes to illustrate the potential extension of the crystalline clusters. A dilation of 5 pixels was found sufficient to obtain objects representative of the crystalline drug clusters identified in the reference raw image data. Further details about this strategy are shown in Figure S5. It should be noted that the pixel size criteria for the dilation operation were based on a subjective segmentation analysis, which can affect the accuracy of the extracted data and subsequent analysis. However, this is a common problem with image analysis, as there is no standard quality indicator (see section 2.2.7).

Fig. 7 illustrates the evolution of the segmented crystalline regions as a function of the drug loading, as well as the main descriptors extracted from the aged samples. The size and total percentage of the segmented crystalline drug domains increased with increasing drug loading as expected due to increasing levels of supersaturation. In specific, at 25 wt% drug loading, the DL50 was 75 µm, at 35 wt% it reached 100 µm and at 50 wt% drug loading the DL50 increased to 160 µm. These crystalline domains were predominantly distributed within the core of the pellets and to a lesser extent in the peripheral sections. The migration of residual crystalline material and/or crystalline nuclei to the centre of the

filament could be attributed to several factors affecting the flow in the die section, including greater flow in the centre of the die/nozzle channel, greater shear rate at the die wall and non-uniform melt temperature profile.

Based on the segmentation analysis, the surface and sub-surface sections of the pellets also displayed a considerable amount of API-rich crystalline clusters, indicating both surface and bulk-mediated API re-crystallisation upon ageing for the supersaturated compositions. The surface API enrichment and crystallisation were confirmed by time-of-flight secondary ion mass spectrometry (ToF-SIMS) analysis and optical microscopy as shown in Fig. 8 (data acquired according to the method described by Paladino *et al.* (Paladino, 2022).

Despite successful identification of the drug crystalline domains in the aged samples (preliminary tests), their detection in the freshly prepared samples was only possible in 50 wt% dispersions processed at 145°C (i.e., lowest processing temperature that contains residual crystallinity according to the phase diagram in Fig. 4.d). This is attributed to detection limitations and size differences between the initial PCM particulates used in the two studies. For the preliminary study a granular grade PCM with a D50 of 378 µm was used, whereas for preparation of the fresh extrudates a powder grade PCM with a D50 of 68 µm was employed. Therefore, even if there is sufficient residual crystalline material to be detected by the other techniques used (i.e., low-frequency Raman, DSC and XRD), their individual particle size is below the lowest Sync-XPC-µCT detection limit when using powdered PCM (0.81 µm/pixel under the present experimental setup). This did not occur for the aged samples because of the larger particle size of the initial material, which along with the time elapsed between ASD manufacture and X-ray imaging enabled further growth to detectable ranges.

3.5. Impurity distribution

In addition to the drug crystalline structures, highly absorbing clusters of material were observed in all samples, regardless of the drug saturation level. These correspond to clusters of NaCl salt, a known impurity present in the polymer (Bordos et al., 2019; Prasad, 2019). The NaCl content was found to be less than 1 %, which is in good agreement with the manufacturer's specifications (< 5 wt%).

Fig. 9.a to 9.f display 3D images highlighting the distribution of this impurity within the pellets. ASDs extruded within the dissolution and suspension regimes were dominated by smaller-diameter NaCl particulates, whilst the systems extruded within the melting regime displayed larger NaCl particulates (see Fig. 9.g to 9.j). This variation is thought to be caused by mechanical breakage of the initial NaCl particles due to higher shear stress and melt viscosity at lower processing temperatures.
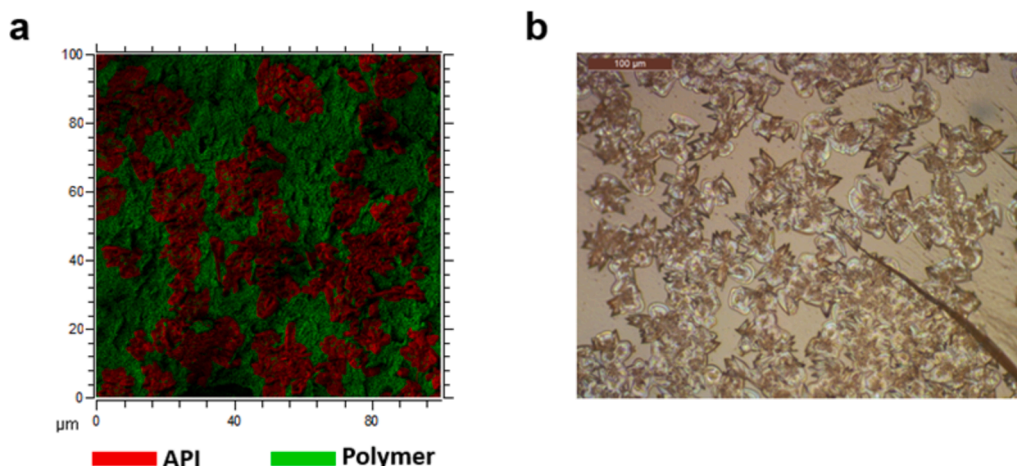

Fig. 8. A) tof-sims chemical imaging and b) optical microscopy illustrating the presence of crystalline api on the surface of the asds.
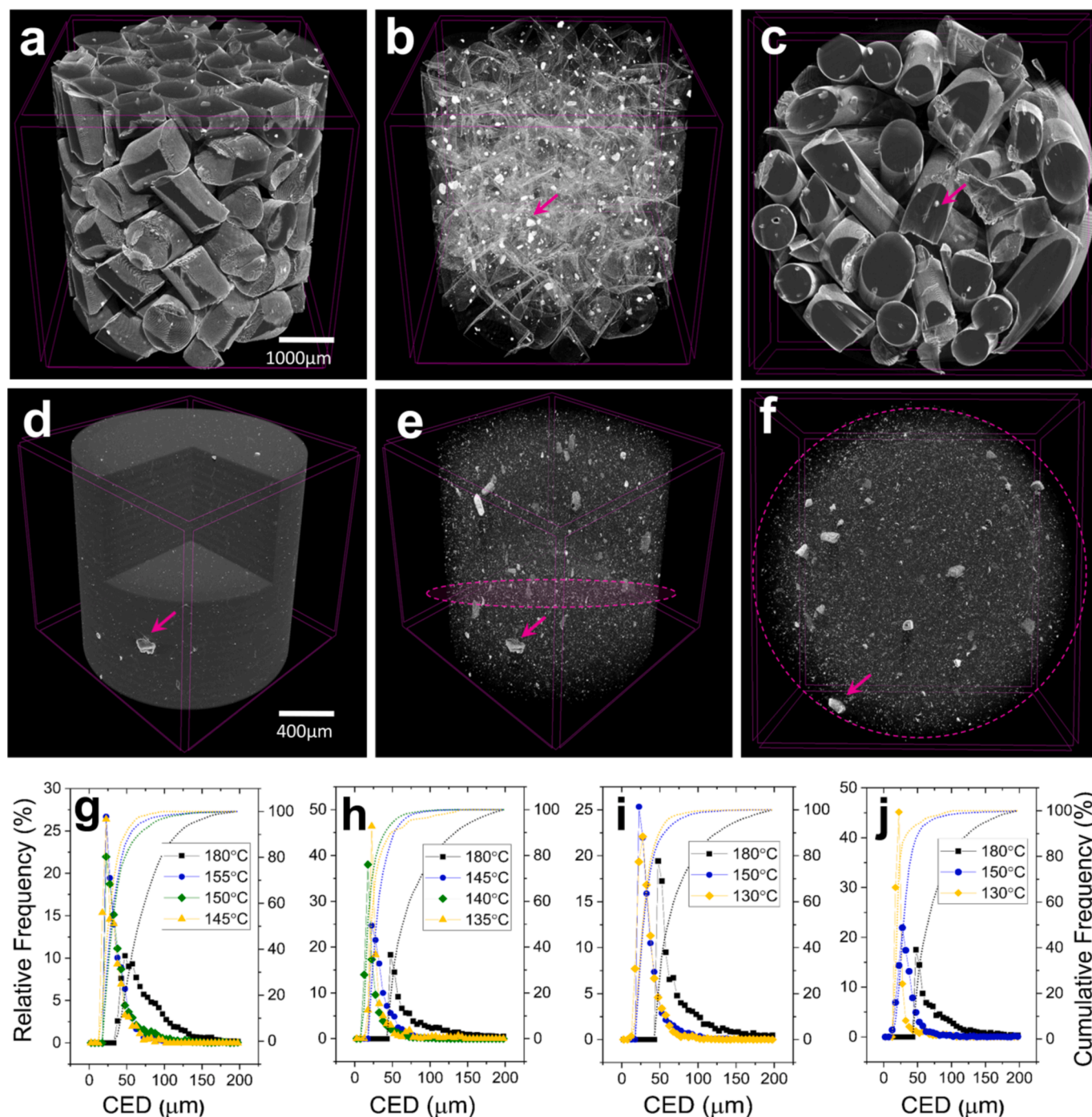
Fig. 9. Representative 3D volume renderings depicting the NaCl clusters from various perspectives: a) to c) 50 wt% drug loading system extruded at 180 °C and d) to f) 10 wt% drug loading system 180 °C. In images b), e) and f) the amorphous matrix was made transparent to highlight the NaCl clusters (denoted by the pink arrows). Size analysis of the NaCl clusters present at g) 50 wt%, h) 35 wt%, i) 20 wt% and j) 10 wt% drug loading (calculated as the circle equivalent diameter, CED).

3.6. Impact of HME processing on the polymer phase homogeneity

The most reported phase separation behaviour in binary ASDs systems is the segregation of the drug from the carrier polymer as either amorphous or crystalline domains (Qi, 2010; Luebbert et al., 2017; Luebbert et al., 2018; Kawakami et al., 2018; Purohit, 2017; Lamm et al., 2016). However, within this study polymer-related heterogeneities (PRH) were found across all systems extruded below the melting point of the drug, as well as in the pure polymer extrudates (i.e., extrudates with no API incorporated). Fig. 10 shows 2D and 3D cross-sections, highlighting droplet and string-shaped structural domains as a function of

the processing temperature and drug loading. Formation of such structures is thought to occur as a result of incomplete softening of the polymer particulates during extrusion. Cellulose derived materials have an intrinsic poor thermal conductivity (Uetani and Hatori, 2017) and the polymer grade used in this study has a high complex viscosity (Gupta et al., 2016) and encompasses a wide range of molecular weights (50–70 kDa), which make the system less plastic, requiring higher temperatures to deform (Khatri et al., 2018; Jain, 2014).

Extrudates prepared under the melting regime lacked the polymer-rich domains and formed homogeneous ASDs. At this temperature, the drug is in the molten state and acts as a "liquid phase", plasticising and
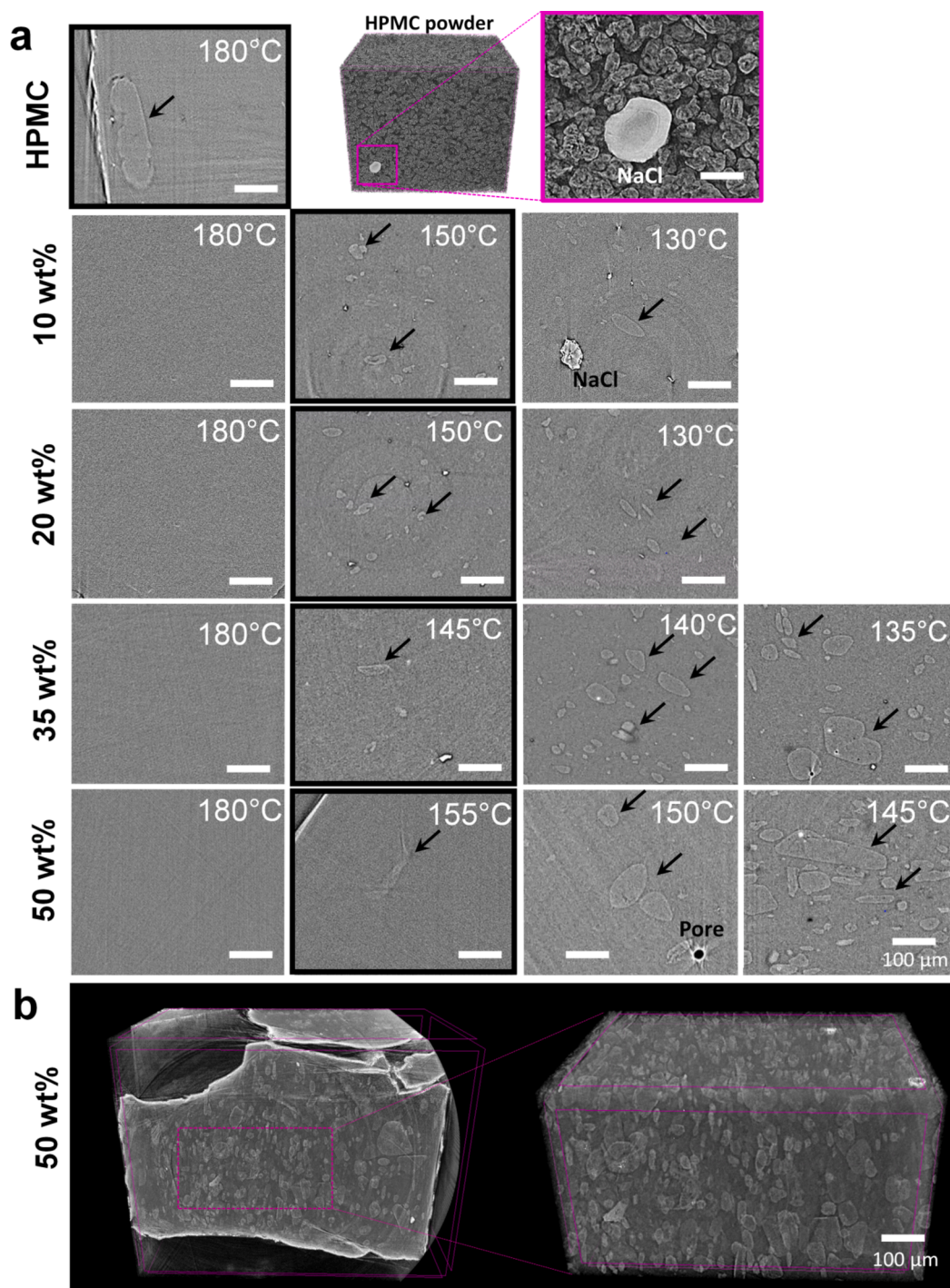
Fig. 10. Impact of HME processing regime and drug loading on the polymer phase homogeneity. a) 2D Cross-sections of all compositions and b) representative 3D volume rendering of the 50 wt% system extruded at 145 °C. The black arrows denote the PRH clusters.

homogenising any unsoften polymer fractions. Upon decreasing the temperature to processing regimes (ii) and (iii), as well as increasing the drug loading, there is a clear increase in the number and size of the polymer-rich domains (ranging from approximately 30 μm to 250 μm). In the dissolution regime, there is no liquid API phase, and therefore, the polymer-related heterogeneities persist. In the suspension regime, the presence of residual drug crystalline particulates exacerbates this tendency by further inhibiting heat propagation within the polymer matrix. Unfortunately, the lack of well-defined borders of these features prevented their segmentation and quantification from the Sync-XPC-μCT data.

Meere et al., predicted similar behaviour in a cellulose-based binary system (Felodipine/HPMCAS) by developing a general multicomponent diffusion model for solid dispersions (Meere et al., 2019). The authors simulated a simplified extrusion process and predicted formation of polymer rich regions at $T_{EXTRUSION} < T_M$, which is in good agreement with our findings. However, this could also occur due to intrinsic miscibility deficiencies.

These results also suggest that further excipients, such as plasticisers, or different screw configuration might be necessary to further refine barrel mixing to prevent the occurrence of the PRH regions in the dissolution regime, at least for highly viscous polymer systems as the one

in this study. However, it should be noted, that while plasticisers would enhance processability, their addition could affect miscibility, decrease the solubility of the API the polymer matrix and increase molecular mobility, thus potentially leading to reduced physical stability.

Moreover, detection of a separated "phase" by DSC is generally described to require the domain size to be of about 30 nm (Padilla, 2011). However, DSC analysis failed to provide any indication of the presence of the polymer-rich domains, which are clearly > 30 nm in dimension. This is likely to occur due to overlapping thermal events but raises questions regarding the DSC phase miscibility indication when only a single T_g is detected.

3.7. Pore fraction analysis

For this type of HME-based ASDs, porosity is generally not created by design but as a by-product of the extrusion process. Although it can be attributed to multiple factors, including air incorporation from the feeding phase, residual humidity and presence of volatile components due to thermal / mechanical degradation or sublimation, its assessment is not routinely performed or reported for this type of drug product. Thus, an in depth qualitative and quantitative structural analysis of the

pore fraction was performed. Fig. 11.a to 11.d display an overlay of the segmented pores and their evolution at different regimes for the 50 wt% drug loading system.

3.7.1. Porosity quantification

Porosity is usually determined in 3D as the pore volumetric percentage, however we sought to investigate whether 2D porosity analysis as the area ratio could be equally used since it is readily obtained from the segmentation process. Results are shown in Fig. 11.e to 11.h. Overall, porosity was found to increase with increasing processing temperature and drug loading, with the 50 wt% system displaying the highest porosity across all processing regimes. The high standard deviation seen in the 2D measurements reflects variations in pore and pellet area between successive tomographic slices, rather than actual porosity changes. Statistical analysis across the temperature-composition space indicates that porosity differences between drug loadings and processing regimes are significant at a significance level of 95 % (see Tables S1 to S3 in the supplementary section). The equivalence of both quantification methods (i.e., in 2D and 3D) is demonstrated by the results in Table S4, where no significant statistical difference was found between the two approaches. Hence, demonstrating porosity determination from the area
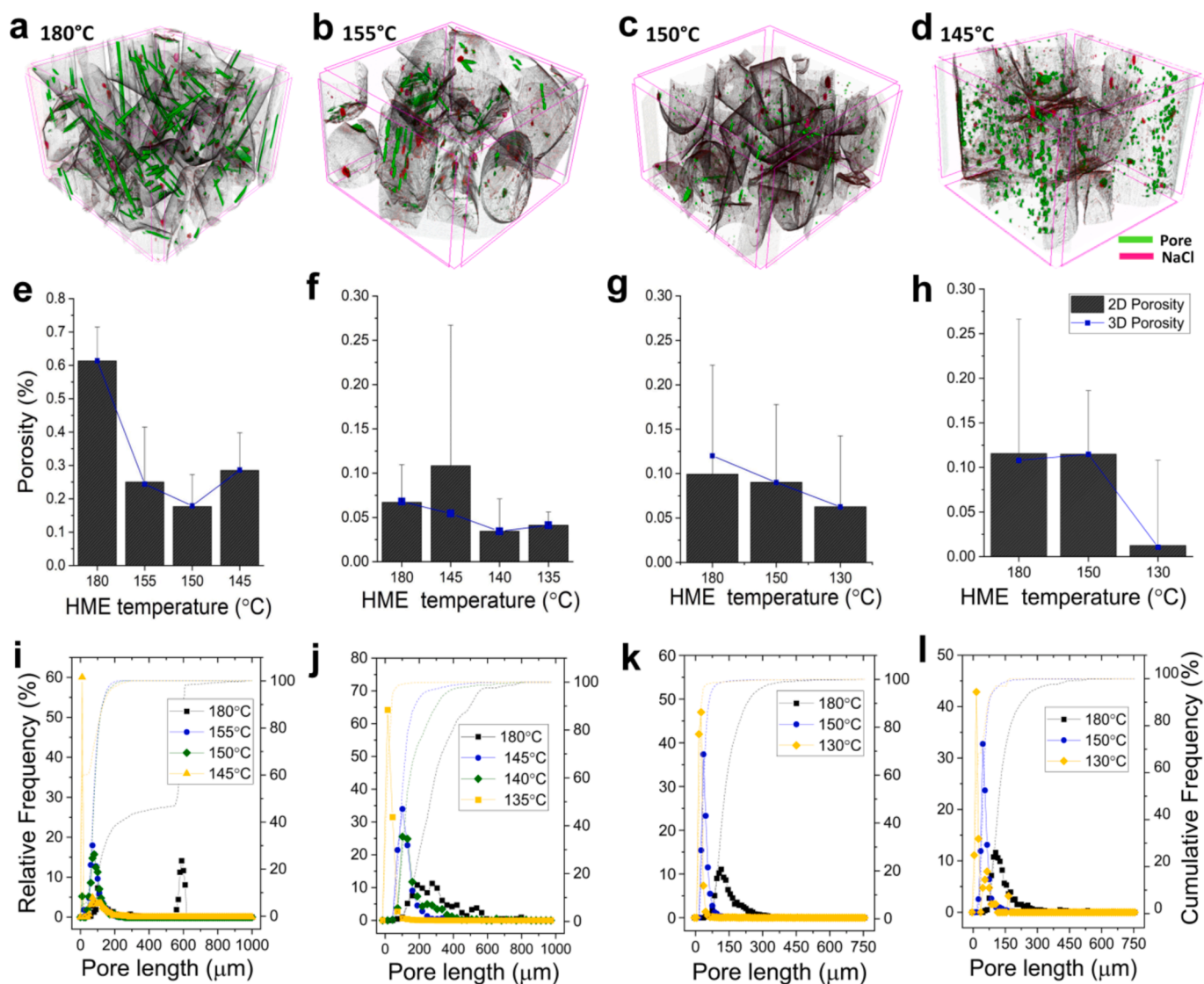

Fig. 11. Segmented pores present within a 4000 x 4000 x 4000 µm volume section present in the 50 wt% system extruded at all three HME regimes: a) melting, b) dissolution and c) and d) suspension regime. 2D and 3D pore quantification at e) 50 wt% drug loading, f) 35 wt%, g) 20 wt% and j) 10 wt% drug loading with the respective pore length from i) to l).

ratio is equally valid.

For the preparation of the aged samples with the 16 mm HME apparatus (i.e., preliminary study), the ventilation window was kept closed and the total porous content was found to vary from ~ 1 % at 10 wt% drug loading, to ~ 10 % 50 wt% drug loading, as displayed in Fig. 8.d. Porosity differences between the two extruding devices (i.e., 16 mm HME used for preparing aged samples and 11 mm HME used for the preparation of fresh samples) may also be driven by additional factors such as the channel fill level and feed rates differences. The higher porous percentage in the high drug loading systems for both devices suggests porosity is mostly drug related. Moisture uptake prior to extrusion, sublimation phenomena during extrusion and the potential release of volatile components as a result degradation might have contributed to the observed trend.

3.7.2. Pore size and shape

The porous network structure was mainly characterised by closed porosity, where discrete occluded pores were dispersed within the ASD matrix without communicating with other pores or the lateral outer surface of the pellets. The pore shape derived from the elongation and flatness ratios of the ellipsoid fitting the pores is presented in Fig. 12 for the 50 wt% system. The pore geometry was found to evolve from predominantly tubular / rod-like shapes at $T_{EXTRUSION} > T_s$ (i.e., melting regime) to a bimodal shape population with tubular and spheroidal pores at $T_{EXTRUSION} < T_s$ (dissolution and suspension regimes). This is also corroborated by the sphericity index values. As expected, spheroidal pores displayed sphericity values closer to 1, while tubular-like pores had lower sphericity values in the 0.1——0.4 range. Typical pore shapes are illustrated in Fig. 12.e. Shape analysis results for the other compositions is shown in Figures S7 to S9 in the supplementary section.

The pore length depicted in Fig. 11.i – 11.L reveals a multi-modal pore size distribution with longer pores present at higher drug loadings and higher processing temperatures. This indicates formation of long tubular porous bodies is favoured within the melting regime and
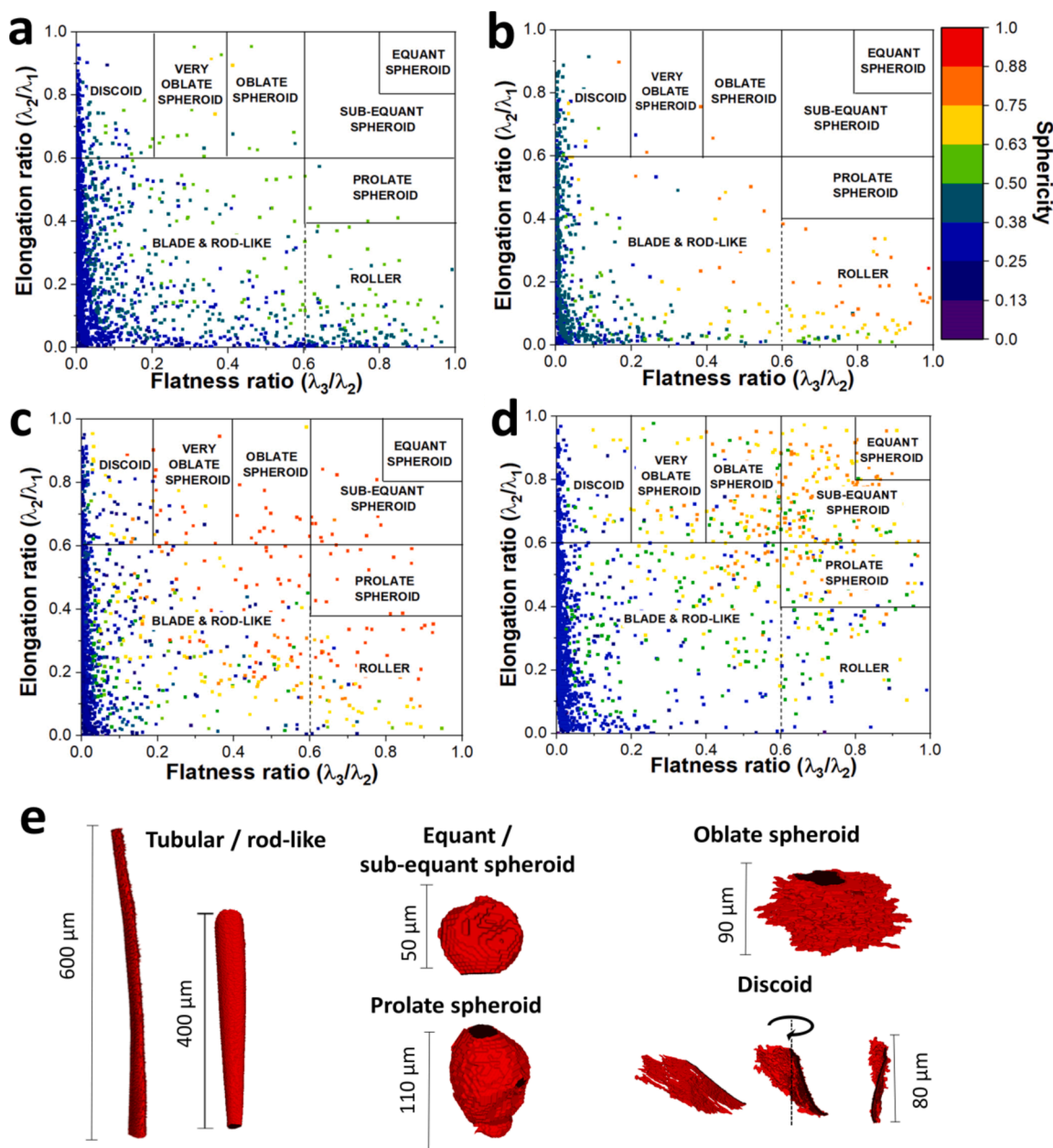

Fig. 12. Shape analysis extracted from the flatness and elongation ratios of the 50 wt% drug loading system extruded at a) 180 °C – melting regime, b) 155 °C – dissolution regime, c) 150 °C and d) 145 °C – suspension regime and e) typical pore shapes.

suggests a gradual pore length decrease within the dissolution and suspension regimes until forming more spheroidal pore shapes in the latter. Changes in pore connectivity, as indicated by consistent trends in length, shape, and diameter variations, are thought to be related to melt viscosity variations during extrusion. As an indirect measure of viscosity, torque was found to decrease with increasing drug loading levels and processing temperatures (data shown in Figure S6). Thus, at $T_{EXTRUSION} > T_s$, formation of tubular porous structures are likely to form through coalescence of minor pores as a result of lower melt viscosity and higher porosity. This is likely to occur within the confines of the die section, where the material accumulates before being forced through the nozzle channel and it is in line with the fluid flow in that section.

3.7.3. Pore orientation

To assess the orientation of the pores, the Euler angles of the eigenvectors describing the ellipsoid fitting the pores were extracted. Fig. 13 shows a preferred orientation within ± 20 degrees (counterclockwise and clockwise, respectively) along the y and z-axis. In conjuction with the visual inspection of the orientation of the pores within the pellets, these results suggest the pore major axis is almost parallel to the direction of the material flow in the extruder.

Furthermore, it is well established in the literature that the inner structure, total porosity, size, shape and pore connectivity can impact the liquid imbibition pattern in pharmaceutical products and affect their dissolution profile, as well as their mechanical properties (Naftaly et al., 2020). These results indicate that this effect could also be extended to ASD products. However, the specific impact of these microstructural differences on the dissolution properties is uncertain as no dissolution tests were carried out. Nonetheless, higher porosity and the presence of open tubular porous structures is likely to have a positive impact by increasing the effective accessible surface area. The presence of pores could also affect the solid-state physical stability by creating a favourable environment for local supersaturation and crystallisation. At the open surface of the pore, the interfacial tension that arises from the surface energy difference between the drug molecules and the surrounding medium can lower the energy barrier for nucleation and promote crystallisation phenomena. In contrast to spray-dried dispersions, which often form spheroidal particles with central voids or honeycomblike structures (Ruprecht et al., 2023; Gamble, 2016; Gamble, 2022), HME-based ASDs tend to be denser with significantly lower porosity (Mahmah et al., 2014). Their smaller surface area is also expected to result in lower moisture uptake, which cumulatively might lead to better physical stability than spray-dried amorphous products despite the presence of pores.

3.8. Surface area measurements by N2 physisorption

As a validating measure of porosity, the ASD surface area was analysed via N_2 gas physisorption. A complex sorption behaviour was observed (see Figure S10), but the overall surface area variation across the temperature-composition space corroborates the general porosity trend derived from the Sync-XPC-μCT image analysis.

4. Discussion

Due to the high temperatures and intensive mixing associated with HME processing, the general assumption is that homogenous ASDs are obtained by default, assuming true thermodynamic equilibrium has been reached. This work adds a new complexity dimension and shows different degrees of heterogeneity across the temperature-composition space. A clear interplay between the HME processing regime, the degree of drug saturation and ASD heterogeneity was found.
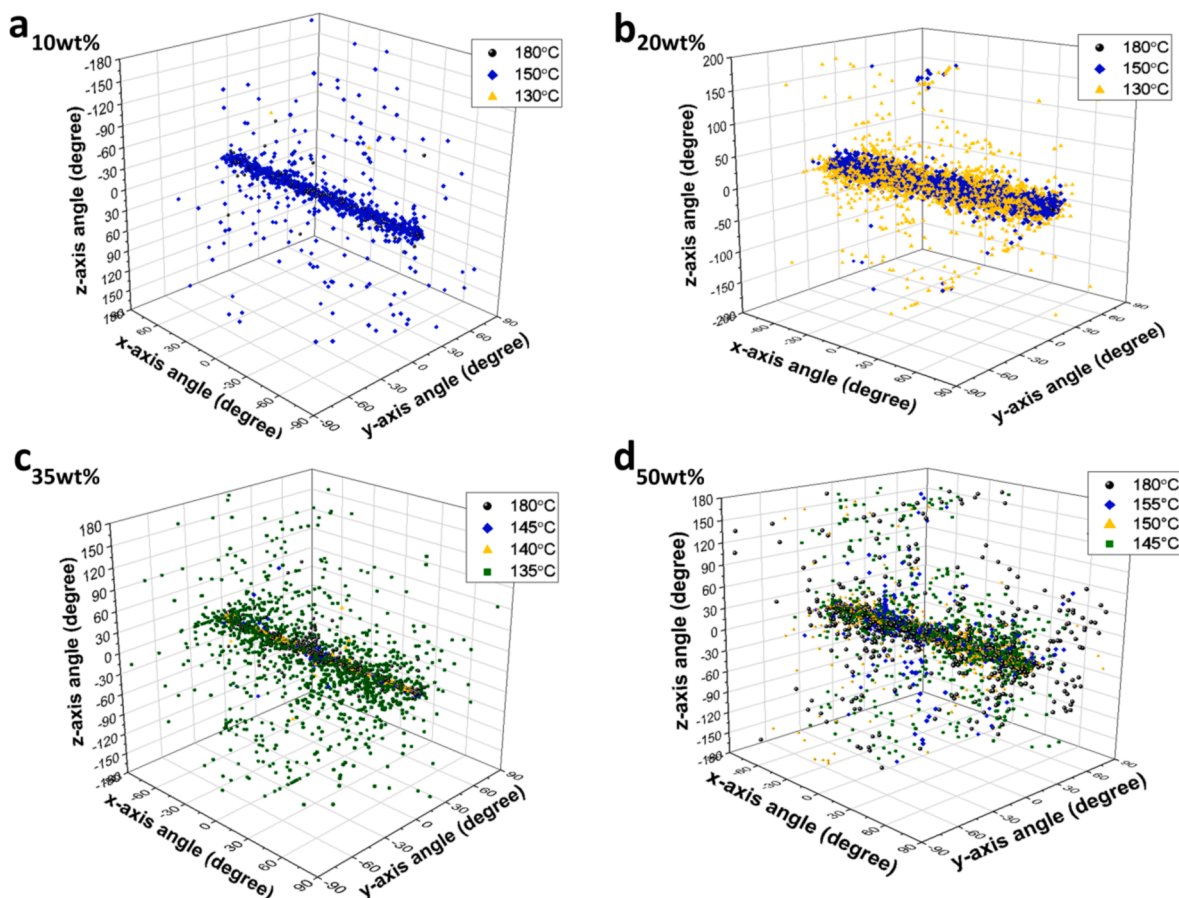

Fig. 13. Pore orientation along the x, y and z axis for the a) 10 wt% system, b) 20 wt% system, c) 35 wt% system and d) 50 wt% system.

The impact of drug saturation was primarily demonstrated in the Sync-XPC-μCT analysis of aged ASDs (6 months old). Even though amorphous ASDs were obtained at the point of manufacture by extruding above the saturated solubility temperature, supersaturated ASDs (> 20 wt% drug loading) were unstable/metastable and exhibited highly defective crystalline API domains upon ageing. The amount and size of these crystalline clusters was found to increase with increasing drug loading, as expected. Conversely, undersaturated ASDs (≤ 20 wt% drug loading) presented better physical stability and lacked the crystalline domains, having a more homogeneous microstructure. Care was taken to include positive control samples in the preliminary study, i.e., samples with residual crystallinity to assure accurate identification of the crystalline domains from the Sync-XPC-μCT data. Porosity also increased with increasing drug loading, suggesting pore formation was at least partially related to volatile materials released from the drug, especially in the melting regime. However, for the non-aged ASDs produced under the melting and dissolution regimes, where the drug is in the amorphous state, additional microstructural differences were observed in terms of pore shape and size, size of the NaCl impurities and presence or absence of polymer-related heterogeneities.

ASDs produced under the melting regime were largely characterised by long tubular pores, whereas the dissolution and suspension regimes presented gradually smaller and more spheroidal pores as temperature decreased. Surprisingly, the HME processing regime had a strong impact on the polymer softening behaviour as well. Polymer-related structural domains were present across all tested coordinates of the API-polymer solubility phase diagram, apart from the melting regime, even though extrusion temperature was still above the polymer's glass transition temperature. It is unclear whether these regions have lower drug content or if they are completely devoid of drug (i.e., comprised by unsoften polymer only), but their presence suggests partial amorphous phase separation and varying local compositions. Further analysis, including chemical imaging, would help elucidate their precise chemical composition, but these results indicate that the polymer's role in ASD heterogeneity warrants additional investigation. Overall, this study demonstrates the need to monitor and investigate other parameters when manufacturing ASDs by HME and not just the absence of residual API crystallinity, as these affect the ASD microstructure and could have a negative impact on product performance and stability. This could have significant implications for pharmaceutical companies that rely on HME for large-scale production.

5. Conclusions

This work demonstrates the potential of synchrotron X-ray phase contrast microtomography (Sync-XPC-μCT) as a tool for the investigation of the internal structure of amorphous solid dispersions (ASDs). In combination with a tailored image analysis strategy, Sync-XPC-μCT provided sufficient contrast to reveal spatially resolved information on the phase distribution homogeneity and existing microstructure within ASDs produced under different saturation conditions. Despite minimal differences in the elemental composition between drug (paracetamol) and polymer (HPMC), which make X-ray absorption contrast imaging difficult, Sync-XPC-μCT revealed multiple structural domains and defects. These include drug-rich crystalline clusters, impurities, polymer-related heterogeneities (PRH) and voids/pores. A clear link between the degree of API saturation and the level of heterogeneity was found. Supersaturated ASDs (> 20 wt% drug loading) displayed higher structural complexity and exhibited a plethora of pores and API-rich crystalline domains upon ageing, which were absent in the undersaturated ASDs. The HME processing regime was found to affect not only residual API crystallinity, but also the pore network structure and the polymer softening behaviour. The presence of polymer-rich domains is indicative of partial amorphous phase separation and varying local compositions, which could have a negative impact on performance and stability.

Overall, this work challenges the belief that HME-based formulations

invariably lead to a homogeneous ASD microstructure, assuming true thermodynamic equilibrium has been attained. Advanced analytical tools, such as Sync-XPC-μCT add a new complexity dimension and reveal different degrees of structural heterogeneity (i.e., level of defects) across the temperature-composition space, even when the drug is already solubilised/amorphous. This suggests that the implications of the API-polymer solubility phase diagram and HME processing regimes extend beyond the crystalline-amorphous dichotomy and can effectively map out the ASD internal microstructure as well. Thus, the combined capabilities of low-frequency Raman and Sync-XPC-μCT provide an effective means of assessing HME performance and efficiency when manufacturing ASDs. In the future, this could be used for the targeted manufacture of stable ASD systems with specific structural and functional features.

Data availability.

All data supporting this study are provided either in the results section of this paper or in the electronic supplementary information accompanying it, except raw Sync-XPC-μCT data which will be made available on request due to large file size.

CRediT authorship contribution statement

Ecaterina Bordos: Writing – original draft, Visualization, Software, Methodology, Investigation, Formal analysis, Data curation, Conceptualization. **Gunjan Das:** Investigation. **Sven L.M. Schroeder:** Writing – review & editing, Visualization, Investigation, Conceptualization. **Alastair Florence:** Supervision, Funding acquisition, Conceptualization. **Gavin W. Halbert:** Writing – review & editing, Visualization, Supervision, Methodology, Conceptualization. **John Robertson:** Writing – review & editing, Visualization, Supervision, Methodology, Investigation, Conceptualization.

Declaration of competing interest

The authors declare that they have no known competing financial interests or personal relationships that could have appeared to influence the work reported in this paper.

Acknowledgements

Appendix A. Supplementary data

Supplementary data to this article can be found online at https://doi.org/10.1016/j.ijpharm.2024.125018.

Data availability

Data will be made available on request.

References

Almotairy, A., et al., 2023. Investigation of hot melt extrusion process parameters on solubility and tabletability of atorvastatin calcium in presence of Neusilin® US2. J. Drug Deliv. Sci. Technol. 79, 104075.

Alzahrani, A., et al., 2022. A systematic and robust assessment of hot-melt extrusion-based amorphous solid dispersions: Theoretical prediction to practical implementation. Int. J. Pharm. 624.

Andrews, G.P., Qian, K., Jacobs, E., Jones, D.S., Tian, Y., 2023. High drug loading nanosized amorphous solid dispersion (NASD) with enhanced in vitro solubility and permeability: Benchmarking conventional ASD. Int. J. Pharm. 632, 122551.

Axelsson, M., Svensson, S., 2010. 3D pore structure characterisation of paper. Pattern Anal. Appl. 13, 159–172.

Bērziņš, K., Fraser-Miller, S.J. & Gordon, K.C. Recent advances in low-frequency Raman spectroscopy for pharmaceutical applications. *International Journal of Pharmaceutics* 120034 Preprint at https://doi.org/10.1016/j.ijpharm.2020.120034 (2020).

Blott, S.J., Pye, K., 2008. Particle shape: A review and new methods of characterization and classification. Sedimentology 55, 31–63.

Bordos, E., Islam, M.T., Florence, A.J., Halbert, G.W., Robertson, J., 2019. Use of Terahertz-Raman Spectroscopy to Determine Solubility of the Crystalline Active Pharmaceutical Ingredient in Polymeric Matrices during Hot Melt Extrusion. Mol. Pharm. 16, 4361–4371.

Butreddy, A., Bandari, S., Repka, M.A., 2021. Quality-by-design in hot melt extrusion based amorphous solid dispersions: An industrial perspective on product development. Eur. J. Pharm. Sci. 158, 105655.

Butreddy, A., Bandari, S., Repka, M.A., 2021. Quality-by-design in hot melt extrusion based amorphous solid dispersions: An industrial perspective on product development. Eur. J. Pharm. Sci. 158.

Croton, L.C.P., et al., 2018. In situ phase contrast X-ray brain CT. Sci. Rep. 8.

Darwich, M., Mohylyuk, V., Kolter, K., Bodmeier, R., Dashevskiy, A., 2023. Enhancement of itraconazole solubility and release by hot-melt extrusion with Soluplus®. J. Drug. Deliv. Sci. Technol. 81, 104280.

Disney, C.M., et al., 2019. Synchrotron tomography of intervertebral disc deformation quantified by digital volume correlation reveals microstructural influence on strain patterns. Acta Biomater. 92, 290–304.

Evans, R.C., et al., 2018. Development and Performance of a Highly Sensitive Model Formulation Based on Torasemide to Enhance Hot-Melt Extrusion Process Understanding and Process Development. AAPS PharmSciTech 19, 1592–1605.

Gamble, J.F., et al., 2016. Application of X-ray microtomography for the characterisation of hollow polymer-stabilised spray dried amorphous dispersion particles. Int. J. Pharm. 510, 1–8.

Gamble, J.F., et al., 2022. Characterization of the Morphological Nature of Hollow Spray Dried Dispersion Particles Using X-ray Submicron-Computed Tomography. AAPS PharmSciTech 23, 1–7.

Giri, B.R., et al., 2021. Hot-Melt Extruded Amorphous Solid Dispersion for Solubility, Stability, and Bioavailability Enhancement of Telmisartan. Pharmaceuticals (Basel) 14, 1–18.

Graeser, K.A., Patterson, J.E., Zeitler, J.A., Rades, T., 2010. The Role of Configurational Entropy in Amorphous Systems. Pharmaceutics 2, 224–244.

Gupta, S.S., Solanki, N., Serajuddin, A.T.M., 2016. Investigation of Thermal and Viscoelastic Properties of Polymers Relevant to Hot Melt Extrusion, IV: Affinisol™ HPMC HME Polymers. AAPS PharmSciTech 17, 148–157.

Hate, S.S., Reutzel-Edens, S.M., Taylor, L.S., 2019. Insight into Amorphous Solid Dispersion Performance by Coupled Dissolution and Membrane Mass Transfer Measurements. Mol. Pharm. 16, 448–461.

Hirling, D. *et al.* Segmentation metric misinterpretations in bioimage analysis. *Nature Methods 2023 21:2* **21**, 213–216 (2023).

Jafarnejad, M., et al., 2019. Quantification of the Whole Lymph Node Vasculature Based on Tomography of the Vessel Corrosion Casts. Sci. Rep. 9, 13380.

Jain, A.K., et al., 2014. The influence of hydroxypropyl methylcellulose (HPMC) molecular weight, concentration and effect of food on in vivo erosion behavior of HPMC matrix tablets. J. Control. Release 187, 50–58.

Kawakami, K., Bi, Y., Yoshihashi, Y., Sugano, K., Terada, K., 2018. Time-dependent phase separation of amorphous solid dispersions: Implications for accelerated stability studies. J. Drug Deliv. Sci. Technol. 46, 197–206.

Khatri, P., Katikaneni, P., Desai, D., Minko, T., 2018. Evaluation of Affinisol® HPMC polymers for direct compression process applications. J. Drug Deliv. Sci. Technol. 47, 461–467.

Kirillov, S.A., Kolomiyets, T.M., 2001. Disorder in binary polymer systems near their critical region studied by low-frequency Raman spectroscopy. J. Phys. Chem. B 105, 3168–3173.

Lamm, M.S., DiNunzio, J., Khawaja, N.N., Crocker, L.S., Pecora, A., 2016. Assessing Mixing Quality of a Copovidone-TPGS Hot Melt Extrusion Process with Atomic Force Microscopy and Differential Scanning Calorimetry. AAPS PharmSciTech 17, 89–98.

Larkin, P.J., Wasylyk, J., Raglione, M., 2015. Application of Low- and Mid-Frequency Raman Spectroscopy to Characterize the Amorphous-Crystalline Transformation of Indomethacin. Appl. Spectrosc. 69, 1217–1228.

Li, P., Batey, D., Rodenburg, J., 2019. An X-ray ptycho-tomography model of 'Seeing order in '''amorphous''''' materials'''''. Ultramicroscopy 203, 88–94.

Li, M., Gogos, C.G., Ioannidis, N., 2015. Improving the API dissolution rate during pharmaceutical hot-melt extrusion I: Effect of the API particle size, and the co-rotating, twin-screw extruder screw configuration on the API dissolution rate. Int. J. Pharm. 478, 103–112.

Li, S., Tian, Y., Jones, D.S., Andrews, G.P., 2016. Optimising Drug Solubilisation in Amorphous Polymer Dispersions: Rational Selection of Hot-melt Extrusion Processing Parameters. AAPS PharmSciTech 17, 200–213.

Luebbert, C., Huxoll, F., Sadowski, G., Van Den Mooter, G., Grohganz, H., 2017. Amorphous-amorphous phase separation in API/polymer formulations. Molecules 22, 1–17.

Luebbert, C., Klanke, C., Sadowski, G., 2018. Investigating phase separation in amorphous solid dispersions via Raman mapping. Int. J. Pharm. 535, 245–252.

Ma, X., et al., 2019. Influence of mechanical and thermal energy on nifedipine amorphous solid dispersions prepared by hot melt extrusion: Preparation and physical stability. Int. J. Pharm. 561, 324–334.

Mahmah, O., Tabbakh, R., Kelly, A., Paradkar, A., 2014. A comparative study of the effect of spray drying and hot melt extrusion on the properties of amorphous solid dispersions containing felodipine. J. Pharm. Pharmacol. 66, 275–284.

Maier-Hein, L. *et al.* Metrics reloaded: recommendations for image analysis validation. *Nature Methods 2024 21:2* **21**, 195–212 (2024).

Marathe, S. *et al.* Development of synchrotron pink beam x-ray grating interferometer at the Diamond Light source I13-2 beamline. in *Developments in X-Ray Tomography XII* (eds. Müller, B. & Wang, G.) vol. 11113 42 (SPIE, 2019).

Markl, D., et al., 2017. Characterization of the Pore Structure of Functionalized Calcium Carbonate Tablets by Terahertz Time-Domain Spectroscopy and X-Ray Computed Microtomography. J. Pharm. Sci. 106, 1586–1595.

Marsac, P.J., Shamblin, S.L., Taylor, L.S., 2006. Theoretical and Practical Approaches for Prediction of Drug-Polymer Miscibility and Solubility. Pharm. Res. 23, 2417–2426.

Marsac, P.J., Li, T., Taylor, L.S., 2009. Estimation of drug-polymer miscibility and solubility in amorphous solid dispersions using experimentally determined interaction parameters. Pharm. Res. https://doi.org/10.1007/s11095-008-9721-1.

Measure properties of 3-D volumetric image regions - MATLAB regionprops3 - MathWorks United Kingdom. https://uk.mathworks.com/help/images/ref/regionprops3.html.

Mayo, S.C., Stevenson, A.W., Wilkins, S.W., 2012. In-Line Phase-Contrast X-ray Imaging and Tomography for Materials Science. Materials 5, 937–965.

Meere, M., Pontrelli, G., McGinty, S., 2019. Modelling phase separation in amorphous solid dispersions. Acta Biomater. 94, 410–424.

Moseson, D.E., et al., 2019. Dissolution of Indomethacin Crystals into a Polymer Melt: Role of Diffusion and Fragmentation. Cryst. Growth Des. 19, 3315–3328.

Moseson, D.E., Taylor, L.S., 2018. The application of temperature-composition phase diagrams for hot melt extrusion processing of amorphous solid dispersions to prevent residual crystallinity. Int. J. Pharm. 553, 454–466.

Moseson, D.E., Taylor, L.S., 2023. Crystallinity: A Complex Critical Quality Attribute of Amorphous Solid Dispersions. Mol. Pharm. 20, 4802–4825.

Naftaly, M., Tikhomirov, I., Hou, P., Markl, D., 2020. Measuring open porosity of porous materials using thz-tds and an index-matching medium. Sensors (switzerland) 20.

Nanubolu, J.B., Burley, J.C., 2012. Investigating the recrystallization behavior of amorphous paracetamol by variable temperature Raman studies and surface raman mapping. Mol. Pharm. 9, 1544–1558.

Nommeots-Nomm, A. *et al.* Four-dimensional imaging and quantification of viscous flow sintering within a 3D printed bioactive glass scaffold using synchrotron X-ray tomography. *Materials Today Advances* vol. 2 (Elsevier, 2019).

Otsu, N., 1979. A Threshold Selection Method from Gray-Level Histograms. IEEE Trans. Syst. Man Cybern. **C** 62–66.

Padilla, A.M., et al., 2011. The Study of Phase Separation in Amorphous Freeze-Dried Systems. Part I: Raman Mapping and Computational Analysis of XRPD Data in Model Polymer Systems. J. Pharm. Sci. 100, 206–222.

Paladino, E., et al., 2022. High spatial resolution ToF-SIMS imaging and image analysis strategies to monitor and quantify early phase separation in amorphous solid dispersions. Int. J. Pharm. 628, 122191.

Patil, H., Tiwari, R.V., Repka, M.A., 2016. Hot-Melt Extrusion: from Theory to Application in Pharmaceutical Formulation. AAPS PharmSciTech 17, 20–42.

Prasad, E., et al., 2019. Development of a hot-melt extrusion (HME) process to produce drug loaded Affinisol™ 15LV filaments for fused filament fabrication (FFF) 3D printing. Addit. Manuf. 29, 100776.

Purohit, H.S., et al., 2017. Insights into Nano- and Micron-Scale Phase Separation in Amorphous Solid Dispersions Using Fluorescence-Based Techniques in Combination with Solid State Nuclear Magnetic Resonance Spectroscopy. Pharm. Res. 34, 1364–1377.

Qi, S., et al., 2010. Characterisation and prediction of phase separation in hot-melt extruded solid dispersions: A thermal, microscopic and NMR relaxometry study. Pharm. Res. 27, 1869–1883.

Rau, C., 2017. Imaging with Coherent Synchrotron Radiation: X-ray Imaging and Coherence Beamline (I13) at Diamond Light Source, Synchrotron Radiation News. Technical. RepoRTs Synchrotron Radiation newS 30, 19–25.

Rau, C. *et al.* Fast Multi-scale imaging using the Beamline I13L at the Diamond Light Source. in *Developments in X-Ray Tomography XII* (eds. Müller, B. & Wang, G.) vol. 11113 68 (SPIE, 2019).

Reinke, A. *et al.* Understanding metric-related pitfalls in image analysis validation. *Nature Methods 2024 21:2* **21**, 182–194 (2024).

Repka, M., Langley, N. & DiNunzio, J. *Melt Extrusion: Materials, Technology and Drug Product Design. Springer* (Springer NewYork Heidelberg Dordrecht London, 2013). doi:10.1007/978-1-4614-8432-5.

Repka, M.A., Majumdar, S., Kumar Battu, S., Srirangam, R., Upadhye, S.B., 2008. Applications of hot-melt extrusion for drug delivery. Expert Opin. Drug Deliv. 5, 1357–1376.

Ruprecht, N.A., Teichmann, H., Kohlus, R., 2023. A particle shape-based segmentation method to characterize spray dried materials by X-Ray microtomography. Particuology 81, 119–127.

Taraskin, S.N., Simdyankin, S.I., Elliott, S.R., Neilson, J.R. & Lo, T. Universal Features of Terahertz Absorption in Disordered Materials. (2006) doi:10.1103/PhysRevLett.97.055504.

Terao, W., et al., 2018. Boson peak dynamics of natural polymer starch investigated by terahertz time-domain spectroscopy and low-frequency Raman scattering. Spectrochim. Acta A Mol. Biomol. Spectrosc. 192, 446–450.

Uetani, K., Hatori, K., 2017. Thermal conductivity analysis and applications of nanocellulose materials. Sci. Technol. Adv. Mater. 18, 877–892.

Van Renterghem, J., et al., 2017. Elucidation and visualization of solid-state transformation and mixing in a pharmaceutical mini hot melt extrusion process using in-line Raman spectroscopy. Int. J. Pharm. 517, 119–127.

Wadeson, N. & Basham, M. Savu: A Python-based, MPI Framework for Simultaneous Processing of Multiple, N-dimensional, Large Tomography Datasets. *arXiv: 1610.08015 [cs]* (2016).

Weitkamp, T., Haas, D., Wegrzynek, D., Rack, A., 2011. ANKAphase: Software for single-distance phase retrieval from inline X-ray phase-contrast radiographs. J. Synchrotron Radiat. 18, 617–629.

Zhang, H., Fritts, J.E., Goldman, S.A., 2008. Image segmentation evaluation: A survey of unsupervised methods. Comput. Vis. Image Underst. 110, 260–280.

Zhao, Y., Inbar, P., Chokshi, H.P., Malick, A.W., Choi, D.S., 2011. Prediction of the thermal phase diagram of amorphous solid dispersions by flory-huggins theory. J. Pharm. Sci. 100, 3196–3207.